Generalized α-attractor models from elementary hyperbolic surfaces

Mirela Babalic, Calin Iuliu Lazaroiu

Center for Geometry and Physics, Institute for Basic Science, Pohang, Republic of Korea 37673

E-mail: mirela@ibs.re.kr, calin@ibs.re.kr

arXiv:1703.01650v2 [hep-th] 4 Apr 2017

Abstract: We consider generalized α-attractor models whose scalar potentials are globally well-behaved and whose scalar manifolds are elementary hyperbolic surfaces. Beyond the Poincaré disk $\mathbb{D}$, such surfaces include the hyperbolic punctured disk $\mathbb{D}^*$ and the hyperbolic annuli $\mathbb{A}(R)$ of modulus $\mu = 2\log R > 0$. For each elementary surface, we discuss its decomposition into canonical end regions and give an explicit construction of the embedding into the Kerekjarto-Stoilow compactification (which in all cases is the unit sphere), showing how this embedding allows for a universal treatment of globally well-behaved scalar potentials upon expanding their extension in real spherical harmonics. For certain simple but natural choices of extended potentials, we compute scalar field trajectories by projecting numerical solutions of the lifted equations of motion from the Poincaré half-plane through the uniformization map, thus illustrating the rich cosmological dynamics of such models.

Contents

1 Generalized α-attractor models **3**
- 1.1 Definition of the models 3
- 1.2 Lift to the Poincaré half-plane 4

2 Laplace expansion of globally well-behaved scalar potentials **5**

3 Elementary hyperbolic surfaces **8**

4 The hyperbolic disk **9**
- 4.1 Semi-geodesic coordinates 9
- 4.2 The end compactification of $\mathbb{D}$ 10
- 4.3 Globally well-behaved scalar potentials on $\mathbb{D}$ 10

5 The hyperbolic punctured disk **12**
- 5.1 The hyperbolic metric 12
- 5.2 Diffeomorphism to the punctured plane 12
- 5.3 Partial isometric embedding into Euclidean 3-space 13
- 5.4 The end compactification of $\mathbb{D}^*$ 13
- 5.5 Semi-geodesic coordinates 13
- 5.6 The hyperbolic cusp 14
- 5.7 The hyperbolic horn 14
- 5.8 Canonical uniformization to $\mathbb{H}$ 14
- 5.9 Canonical uniformization to $\mathbb{D}$ 15
- 5.10 Globally well-behaved scalar potentials on $\mathbb{D}^*$ 16
- 5.11 Cosmological trajectories on the hyperbolic punctured disk 18

6 Hyperbolic annuli **22**
- 6.1 The hyperbolic metric 22
- 6.2 Diffeomorphism to the punctured disk and to the punctured plane 23
- 6.3 The end compactification of $\mathbb{A}(R)$ 23
- 6.4 The hyperbolic funnel 24
- 6.5 Semi-geodesic coordinates on F_ℓ 24
- 6.6 Partial isometric embedding of the funnel into Euclidean 3-space 25
- 6.7 Canonical uniformization to $\mathbb{H}$ 25
- 6.8 Canonical uniformization to $\mathbb{D}$ 26
- 6.9 Globally well-behaved scalar potentials on $\mathbb{A}(R)$ 27
- 6.10 Lift of the cosmological model to $\mathbb{H}$ 31

7 Conclusions and further directions **35**

Introduction

In [1], we introduced a class of cosmological models which form a wide generalization of α-attractors [2–7]. Such models are defined by cosmological solutions (with flat spatial section) of the Einstein theory of gravity coupled to two real scalar fields, the dynamics of the latter being described by a non-linear sigma model whose scalar manifold is a non-compact, oriented and topologically finite borderless surface Σ endowed with a complete metric $\mathcal{G}$ of constant Gaussian curvature $K = -\frac{1}{3\alpha}$. The scalar potential is given by a smooth real-valued function Φ defined on Σ. The rescaled scalar field metric $G \stackrel{\text{def.}}{=} \frac{1}{3\alpha}\mathcal{G}$ has Gaussian curvature equal to -1, hence (Σ, G) is a geometrically finite hyperbolic surface in the sense of [8]. Using the uniformization theorem of Koebe and Poincaré [9] and the theory of surface groups (Fuchsian groups without elliptic elements), reference [1] discussed the basic features of cosmological dynamics and inflation in such models.

In the present paper, we consider the non-generic situation when (Σ, G) is elementary, focusing on special features which arise in this case. As explained in [1], an elementary hyperbolic surface (Σ, G) is isometric with the hyperbolic disk $\mathbb{D}$, with the hyperbolic punctured disk $\mathbb{D}^*$ or with the hyperbolic annulus $\mathbb{A}(R)$ of modulus $\mu = 2\log R$, where $R > 1$ is a real number. Each of these surfaces is planar, having the unit sphere S^2 as its end compactification. This allows one to parameterize globally well-behaved [1] scalar potentials Φ through the coefficients of the Laplace expansion of their global extension $\hat{\Phi}$ to the end compactification, which in this case reduces to an expansion in real spherical harmonics. Both the hyperbolic metric and a fundamental polygon are known explicitly for $\mathbb{D}^*$ and $\mathbb{A}(R)$. In particular, one can describe explicitly the hyperbolic geometry of such surfaces and one can compute scalar field trajectories on $(\Sigma, \mathcal{G})$ by determining trajectories of an appropriate lift of the model to the Poincaré half-plane $\mathbb{H}$ and projecting them to $\mathbb{D}^*$ or to $\mathbb{A}(R)$ through the uniformization map. When the scalar potential is constant, this illustrates how the different projections from $\mathbb{H}$ to $\mathbb{D}^*$ and $\mathbb{A}(R)$ can take the same trajectory on the Poincaré half-plane into qualitatively different trajectories on the corresponding elementary hyperbolic surface. The explicit embeddings of $\mathbb{D}$, $\mathbb{D}^*$ and $\mathbb{A}(R)$ into their common Kerekjarto-Stoilow compactification S^2 are also different. As a consequence, a smooth real-valued function defined on S^2 will generally induce rather different globally well-behaved scalar potentials on the disk, the punctured disk and the annulus. When combined with the different projections from $\mathbb{H}$, this leads to qualitatively different dynamics on $\mathbb{D}$, $\mathbb{D}^*$ and $\mathbb{A}(R)$. By considering some simple but natural choices of extended scalar potentials on S^2, we use numerical methods to compute various trajectories on $\mathbb{D}^*$ and $\mathbb{A}(R)$, thus illustrating the rich dynamics of such models, which is not entirely visible in the gradient flow approximation.

The paper is organized as follows. Section 1 briefly recalls the definition of generalized α-attractor models and the lift of their cosmological evolution equation to the Poincaré half-plane. In Section 2, we consider globally well-behaved scalar potentials on topologically-finite planar oriented surfaces (of which the elementary surfaces are particular cases), showing how they can be parameterized through the coefficients of the Laplace expansion of their extension to the end compactification. In Section 3, we review the classification of elemen-

tary hyperbolic surfaces and some of their basic properties. Section 4 recalls the case of the hyperbolic disk, showing how it fits into the general approach developed in [1] and how well-behaved scalar potentials can be described through the Laplace expansion of their extension to S^2. Section 5 discusses the hyperbolic punctured disk. After giving the explicit form of the hyperbolic metric on $\mathbb{D}^*$, of a partial isometric embedding into three-dimensional Euclidean space and of the decomposition into horn and cusp regions, we compute certain scalar field trajectories for a few globally well-behaved scalar potentials which are induced naturally from S^2. Section 6 performs a similar analysis for hyperbolic annuli, using globally well-behaved scalar potentials induced by the same choices of functions on S^2. In particular, this illustrates how the dynamics of our models differs on $\mathbb{A}(R)$ and $\mathbb{D}^*$. Section 7 contains our conclusions and sketches a few directions for further research.

Notations and conventions. All manifolds considered are smooth, connected, oriented and paracompact (hence also second-countable). All homeomorphisms and diffeomorphisms considered are orientation-preserving. By definition, a Lorentzian four-manifold has "mostly plus" signature. The symbol $\mathbf{i}$ denotes the imaginary unit. The Poincaré half-plane is the upper half plane with complex coordinate τ:

$$\mathbb{H} = \{\tau \in \mathbb{C} \,|\, \mathrm{Im}\tau > 0\} \quad , \tag{0.1}$$

endowed with its unique complete metric of Gaussian curvature -1, which is given by:

$$\mathrm{d}s^2_{\mathbb{H}} = \frac{1}{(\mathrm{Im}\tau)^2}|\mathrm{d}\tau|^2 \quad .$$

The real coordinates on $\mathbb{H}$ are denoted by $x \overset{\text{def.}}{=} \mathrm{Re}\tau$ and $y \overset{\text{def.}}{=} \mathrm{Im}\tau$. The complex coordinate on the hyperbolic disk, the hyperbolic punctured disk or an annulus is denoted by u. We define the *rescaled Planck mass* through:

$$M_0 \overset{\text{def.}}{=} M\sqrt{\frac{2}{3}} \quad , \tag{0.2}$$

where M is the (reduced) Planck mass.

1 Generalized α-attractor models

1.1 Definition of the models

Let (Σ, G) be a non-compact borderless, oriented, connected and complete two-dimensional Riemannian manifold (called the *scalar manifold*) and $\Phi : \Sigma \to \mathbb{R}$ be a smooth function (called the *scalar potential*). We say that (Σ, G) is *hyperbolic* if the metric G has constant Gaussian curvature equal to -1. We assume that the fundamental group $\pi_1(\Sigma)$ is finitely-generated, which means that Σ is *topologically finite* and that (Σ, G) is *geometrically finite*. Let $\mathcal{G} = 3\alpha G$, where $\alpha > 0$ is a fixed positive real number.

Let X be any four-manifold which can support Lorentzian metrics. The Einstein-Scalar theory defined by the triplet $(\Sigma, \mathcal{G}, \Phi)$ includes four-dimensional gravity (described

by a Lorentzian metric g defined on X) and a smooth map $\varphi : X \to \Sigma$, with action [1]:

$$S[g,\varphi] = \int_X \left[\frac{M^2}{2}\mathrm{R}(g) - \frac{1}{2}\mathrm{Tr}_g\varphi^*(\mathcal{G}) - \Phi\circ\varphi\right]\mathrm{vol}_g \quad . \tag{1.1}$$

Here vol_g is the volume form of (X,g), $\mathrm{R}(g)$ is the scalar curvature of g and M is the (reduced) Planck mass.

When X is diffeomorphic with $\mathbb{R}^4$ and g is a FLRW metric with flat spatial section, solutions of the equations of motion for the action (1.1) for which φ depends only on the cosmological time t define the class of so-called *generalized α-attractor models* [1]. In this case, the map $\mathfrak{I} \ni t \to \varphi(t) \in \Sigma$ (where $\mathfrak{I}$ is a real interval) defines a curve in Σ which obeys an invariantly-defined non-linear second order ordinary differential equation (which is locally equivalent with a system of two second order equations). We refer the reader to [1] for a general discussion of such models.

1.2 Lift to the Poincaré half-plane

As explained in [1], the cosmological equations of motion can be lifted from Σ to the Poincaré half-plane $\mathbb{H}$ by using the covering map $\pi_{\mathbb{H}} : \mathbb{H} \to \Sigma$ which uniformizes (Σ, G) to $\mathbb{H}$. This allows one to determine the cosmological trajectories $\varphi(t)$ by projecting trajectories $\tilde{\varphi}(t)$ of a "lifted" model defined on $\mathbb{H}$. The lifted model is governed by the following system of second order non-linear ordinary differential equations [1, eq. (7.4)]:

$$\begin{aligned}
&\ddot{x} - \frac{2}{y}\dot{x}\dot{y} + \frac{1}{M}\sqrt{\frac{3}{2}}\left[3\alpha\frac{\dot{x}^2+\dot{y}^2}{y^2} + 2\tilde{\Phi}(x,y)\right]^{1/2}\dot{x} + \frac{1}{3\alpha}y^2\partial_x\tilde{\Phi}(x,y) = 0 \\
&\ddot{y} + \frac{1}{y}(\dot{x}^2-\dot{y}^2) + \frac{1}{M}\sqrt{\frac{3}{2}}\left[3\alpha\frac{\dot{x}^2+\dot{y}^2}{y^2} + 2\tilde{\Phi}(x,y)\right]^{1/2}\dot{y} + \frac{1}{3\alpha}y^2\partial_y\tilde{\Phi}(x,y) = 0 \quad ,
\end{aligned} \tag{1.2}$$

where $\dot{} \overset{\text{def.}}{=} \frac{\mathrm{d}}{\mathrm{d}t}$ and $x = \mathrm{Re}\tau$, $y = \mathrm{Im}\tau$ are the Cartesian coordinates on the Poincaré half plane with complex coordinate τ and $\tilde{\Phi} \overset{\text{def.}}{=} \Phi\circ\pi_{\mathbb{H}} : \mathbb{H} \to \mathbb{R}$ is the *lifted potential*. Let u_0 be any point of Σ and let $\tau_0 \in \mathbb{H}$ be chosen such that $\pi_{\mathbb{H}}(\tau_0) = u_0$. An initial velocity vector $v_0 = \dot{u}_0 \in T_{u_0}\Sigma$ defined at u_0 on $\mathbb{D}^*$ and its unique lift $\tilde{v}_0 = \dot{\tau}_0 \in T_{\tau_0}\mathbb{H}$ through the differential[1] of $\pi_{\mathbb{H}}$ at τ_0 are related through:

$$v_0 = (\mathrm{d}_{\tau_0}\pi_{\mathbb{H}})(\tilde{v}_0) \quad .$$

Writing $\tau = x + \mathbf{i}y$ and $\tau_0 = x_0 + \mathbf{i}y_0$, we have $\tilde{v}_0 = \tilde{v}_{0x} + \mathbf{i}\tilde{v}_{0y}$ with real $\tilde{v}_{0x}$, $\tilde{v}_{0y}$. As shown in [1], a cosmological trajectory $\varphi(t)$ on Σ with initial condition (u_0,τ_0) can be written as $\varphi(t) = \pi_{\mathbb{H}}(\tilde{\varphi}(t))$, where $\tilde{\varphi}(t) = x(t) + \mathbf{i}y(t)$ is the solution of the lifted system (1.2) with initial conditions:

$$x(0) = x_0 \quad , \quad y(0) = y_0 \quad \text{and} \quad \dot{x}(0) = \tilde{v}_{0x} \quad , \quad \dot{y}(0) = \tilde{v}_{0y} \quad .$$

[1]Notice that the differential of $\pi_{\mathbb{H}}$ at τ_0 is a bijective linear map because $\pi_{\mathbb{H}}$ is a covering map and hence a local diffeomorphism.

Eliminating the Planck mass. Let $\tilde{\mathbf{\Phi}} = \frac{1}{M_0}\tilde{\Phi}$ and $\boldsymbol{\alpha} = \frac{1}{M_0}\alpha$, where $M_0 = M\sqrt{\frac{2}{3}}$ is the rescaled Planck mass (0.2). Then (1.2) becomes:

$$\ddot{x} - \frac{2}{y}\dot{x}\dot{y} + \left[3\boldsymbol{\alpha}\frac{\dot{x}^2+\dot{y}^2}{y^2} + 2\tilde{\mathbf{\Phi}}(x,y)\right]^{1/2}\dot{x} + \frac{1}{3\boldsymbol{\alpha}}y^2\partial_x\tilde{\mathbf{\Phi}}(x,y) = 0$$
$$\ddot{y} + \frac{1}{y}(\dot{x}^2-\dot{y}^2) + \left[3\boldsymbol{\alpha}\frac{\dot{x}^2+\dot{y}^2}{y^2} + 2\tilde{\mathbf{\Phi}}(x,y)\right]^{1/2}\dot{y} + \frac{1}{3\boldsymbol{\alpha}}y^2\partial_y\tilde{\mathbf{\Phi}}(x,y) = 0 \quad , \qquad (1.3)$$

showing that we can eliminate the Planck mass from the equations provided that we measure both α and $\tilde{\Phi}$ (and hence also Φ) in units of M_0. The numerical solutions extracted in latter sections of this paper were obtained using the system (1.3), after performing such a rescaling of α and Φ.

2 Laplace expansion of globally well-behaved scalar potentials

Let $\hat{\Sigma}$ denote the Kerekjarto-Stoilow (a.k.a. end) compactification of Σ (see [10, 11]) and identify Σ with its image in $\hat{\Sigma}$ through the embedding map $j : \Sigma \to \hat{\Sigma}$. A smooth scalar potential $\Phi : \Sigma \to \mathbb{R}$ is called *globally well-behaved* [1] if there exists a smooth function $\hat{\Phi} : \hat{\Sigma} \to \mathbb{R}$ whose restriction to Σ equals Φ; in this case, $\hat{\Phi}$ is uniquely determined by Φ through continuity. Since all elementary hyperbolic surfaces (Σ, G) are planar, their end compactification $\hat{\Sigma}$ is diffeomorphic with the unit sphere $\mathrm{S}^2 = \{(x_1,x_2,x_3) \in \mathbb{R}^3 \,|\, x_1^2 + x_2^2 + x_3^2 = 1\}$, so in this case globally well-defined scalar potentials on Σ correspond bijectively to smooth functions $\hat{\Phi} : \mathrm{S}^2 \to \mathbb{R}$.

Let ψ and θ be spherical coordinates on S^2, thus:

$$x_1 = \sin\psi\cos\theta \quad , \quad x_2 = \sin\psi\sin\theta \quad , \quad x_3 = \cos\psi \quad , \qquad (2.1)$$

where $\psi \in [0,\pi]$ and $\theta \in [0, 2\pi)$. Any smooth map $\hat{\Phi} : \mathrm{S}^2 \to \mathbb{R}$ is square-integrable with respect to the round Lebesgue measure $\sin\psi \mathrm{d}\psi\mathrm{d}\theta$ on S^2 and admits the Laplace-Fourier series expansion:

$$\hat{\Phi}(\psi,\theta) = \sum_{l=0}^{\infty}\sum_{m=-l}^{l} C_{lm}Y_l^m(\psi,\theta) \quad , \qquad (2.2)$$

where Y_l^m are the complex spherical harmonics and:

$$C_{lm} = \int_{\mathrm{S}^2} \mathrm{d}\psi\mathrm{d}\theta \sin\psi \overline{Y_l^m(\psi,\theta)}\hat{\Phi}(\psi,\theta) \in \mathbb{C} \quad .$$

The series in (2.2) converges *uniformly* to $\hat{\Phi}$ on S^2 since $\hat{\Phi}$ is smooth (see [12]). Recall that $Y_l^m(\psi,\theta) = P_l^m(\cos\psi)e^{\mathbf{i}m\theta}$, where $P_l^m(x)$ are the associated Legendre functions. Since $\hat{\Phi}$ is real-valued, expansion (2.2) reduces to:

$$\hat{\Phi}(\psi,\theta) = \sum_{l=0}^{\infty}\sum_{m=-l}^{l} P_l^m(\cos\psi)[A_{lm}\cos(m\theta) + B_{lm}\sin(m\theta)]$$

where A_{lm} and B_{lm} are real constants. Equivalently, we have:

$$\hat{\Phi}(\psi,\theta) = \sum_{l=0}^{\infty} \sum_{m=-l}^{l} D_{lm} Y_{lm}(\psi,\theta) \quad , \tag{2.3}$$

where $D_{lm} \in \mathbb{R}$ and Y_{lm} are the real (a.k.a. tesseral) spherical harmonics, which correspond to orbitals. This expansion is again uniformly-convergent and gives a systematic way to approximate $\hat{\Phi}$ by truncating away the contributions with l greater than some cutoff value.

Some particular choices for $\hat{\Phi}$. If only the modes with $l = 0$ and $l = 1$ (s and p orbitals) are present, then we have:

$$\hat{\Phi}(\psi,\theta) = a + b\cos\psi + c\sin\psi\cos\theta + d\sin\psi\sin\theta \quad , \tag{2.4}$$

where a, b, c, d are real constants and we used the expressions:

$$P_0^0(x) = 1 \quad , \quad P_1^0(x) = x \quad , \quad P_1^1(x) = -\sqrt{1-x^2} \quad , \quad P_1^{-1}(x) = \frac{1}{2}\sqrt{1-x^2}$$

$$Y_{00} = \frac{1}{2\sqrt{\pi}} \quad , \quad Y_{10} = \sqrt{\frac{3}{4\pi}}\cos\psi \quad , \quad Y_{11} = \sqrt{\frac{3}{4\pi}}\sin\psi\cos\theta \quad , \quad Y_{1,-1} = \sqrt{\frac{3}{4\pi}}\sin\psi\sin\theta \quad .$$

The constant term in (2.4) corresponds to the s orbital (Y_{00}) while the terms with prefactors b, c and d correspond to the orbitals p_z (Y_{10}), p_x (Y_{11}) and p_y ($Y_{1,-1}$).

For $c = d = 0$, two simple choices are $a = b = \frac{1}{2}M_0$ and $a = -b = \frac{1}{2}M_0$, where M_0 is the rescaled Planck mass (0.2). These give the following θ-independent potentials, which involve only the orbitals s and p_z and are shown in Figure 1:

$$\hat{\Phi}_+(\psi) = M_0\cos^2\left(\frac{\psi}{2}\right) \quad , \quad \hat{\Phi}_-(\psi) = M_0\sin^2\left(\frac{\psi}{2}\right) \quad . \tag{2.5}$$

Notice that $\hat{\Phi}_+$ has a maximum at $\psi = 0$ (north pole) and a minimum at $\psi = \pi$ (south pole) while $\hat{\Phi}_-$ has a minimum at $\psi = 0$ (north pole) and a maximum at $\psi = \pi$ (south pole).

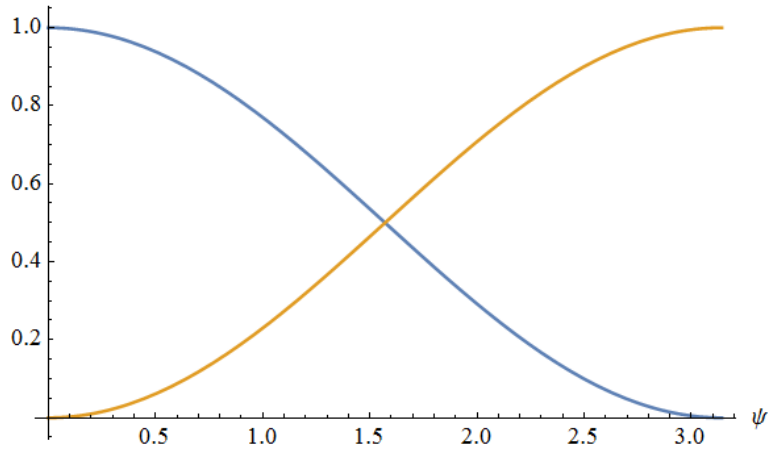

Figure 1: Plot of $\hat{\Phi}_+/M_0$ (blue) and $\hat{\Phi}_-/M_0$ (yellow) as functions of $\psi \in [0,\pi]$. The value $\psi = 0$ corresponds to the north pole of S^2, while $\psi = \pi$ corresponds to the south pole.

Another simple choice is $b = d = 0$ and $a = c := M_0$, which corresponds to a linear combination of the s and p_x orbitals and gives the extended potential:

$$\hat{\Phi}_0(\psi, \theta) = M_0(1 + \sin\psi\cos\theta) = M_0(1 + x_1) \quad . \tag{2.6}$$

Unlike $\hat{\Phi}_\pm$, this function does not have extrema at the north or south pole. Instead, it has two extrema along the equator of S^2, having a maximum (equal to $2M_0$) at the point $(\psi, \theta) = (\frac{\pi}{2}, 0)$ and a minimum (equal to 0) at $(\psi, \theta) = (\frac{\pi}{2}, \pi)$. Notice that $\hat{\Phi}_\pm$ and $\hat{\Phi}_0$ are Morse functions on S^2, so the potentials derived from them on a planar surface (whose end compactification is S^2) will be compactly Morse in the sense of [1].

A universal approach to globally well-behaved potentials. The techniques of passing to the end compactification and lifting to the Poincaré half-plane introduced in [1] allow for a uniform treatment of globally well-behaved scalar potentials in generalized α-attractor models for which (Σ, G) is geometrically finite. This is summarized in the commutative diagram (2.7), where j is the smooth embedding of Σ into its end compactification $\hat{\Sigma}$ and $\pi_{\mathbb{H}}$ is the uniformizing map from $\mathbb{H}$.

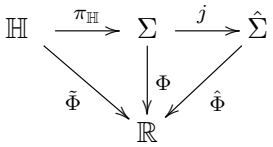

(2.7)

Any smooth real-valued function $\hat{\Phi}$ defined on $\hat{\Sigma}$ induces a globally well-behaved scalar potential Φ on Σ through the formula $\Phi = \hat{\Phi} \circ j$, while any globally well-behaved scalar potential Φ on Σ lifts to a smooth function $\tilde{\Phi} = \Phi \circ \pi_{\mathbb{H}}$ defined on $\mathbb{H}$. When the maps j and $\pi_{\mathbb{H}}$ are known, $\tilde{\Phi}$ can be recovered from $\hat{\Phi}$ as the composition $\tilde{\Phi} = \hat{\Phi} \circ \chi$, where $\chi : \mathbb{H} \to \hat{\Sigma}$ is the composite map $\chi \overset{\text{def.}}{=} j \circ \pi_{\mathbb{H}}$. Notice that j and χ are smooth maps, while $\pi_{\mathbb{H}}$ is holomorphic when Σ is endowed with the complex structure which corresponds to the conformal class of the metric G. The maps $j, \pi_{\mathbb{H}}$ and χ differ for distinct geometrically-finite hyperbolic surfaces $(\hat{\Sigma}, G)$ having the same end compactification $\hat{\Sigma}$, which means that the same "universal" extended potential $\hat{\Phi}$ defined on $\hat{\Sigma}$ can induce markedly different globally well-behaved potentials Φ and lifted potentials $\tilde{\Phi}$ for different hyperbolic surfaces of the same genus.

When Σ is a planar surface, the end compactification $\hat{\Sigma}$ coincides with the unit sphere and $\hat{\Phi}$ can be expanded into real spherical harmonics as explained above. This induces uniformly-convergent expansions:

$$\Phi = \sum_{l=0}^{\infty} \sum_{m=-l}^{l} D_{lm} Y_{lm} \circ j$$

$$\tilde{\Phi} = \sum_{l=0}^{\infty} \sum_{m=-l}^{l} D_{lm} Y_{lm} \circ \chi$$

of Φ and $\tilde{\Phi}$. In the next sections, we determine explicitly the maps j, $\pi_{\mathbb{H}}$ and χ for the planar elementary surfaces $\mathbb{D}$, $\mathbb{D}^*$ and $\mathbb{A}(R)$ and the maps Φ and $\tilde{\Phi}$ induced by the

choices $\hat{\Phi} = \hat{\Phi}_{\pm}$ and $\hat{\Phi} = \hat{\Phi}_0$ given above. This illustrates how the same function $\hat{\Phi}$ leads to different dynamics of the generalized α-attractor models associated to distinct planar surfaces. For the three elementary surfaces, we will construct the map $j : \Sigma \to \hat{\Sigma} = \mathrm{S}^2$ by first diffeomorphically (but not bi-holomorphically !) identifying Σ with the complex plane $\mathbb{C}$ of complex coordinate ζ (or with $\mathbb{C}$ with a point removed) and then identifying the latter with the once- or twice-punctured sphere using stereographic projection from the north pole of S^2:

$$\zeta = \cot\left(\frac{\psi}{2}\right) e^{\mathbf{i}\theta} \in \mathbb{C} \quad . \tag{2.8}$$

3 Elementary hyperbolic surfaces

A (complete) hyperbolic surface (Σ, G) is called *elementary* if it is conformally-equivalent with a simply-connected or doubly-connected regular domain contained in the complex plane[2]. This amounts to the condition that the uniformizing surface group Γ of (Σ, G) is the trivial group or a cyclic subgroup of $\mathrm{PSL}(2, \mathbb{R})$ of parabolic or hyperbolic type.

Any simply connected regular domain is conformally equivalent with the unit disk $\mathbb{D} = \{u \in \mathbb{C} \,|\, |u| < 1\}$ (and hence with the upper half plane $\mathbb{H}$). Such a domain admits a unique complete hyperbolic metric, known as the Poincaré metric. Any doubly-connected regular domain is conformally equivalent to one of the following, when the latter is endowed with the complex structure inherited from the complex plane:

- The punctured plane $\mathbb{C}^* = \mathbb{C} \setminus \{0\}$
- The punctured unit disk $\mathbb{D}^* \stackrel{\text{def.}}{=} \mathbb{D} \setminus \{0\}$
- The annulus $\mathbb{A}(R) \stackrel{\text{def.}}{=} \{u \in \mathbb{C} \mid \frac{1}{R} < |u| < R\}$ of modulus $\mu = 2 \log R > 0$, where $R > 1$.

When endowed with its usual complex structure, the punctured plane does not support a complete hyperbolic metric. On the other hand, the punctured disk $\mathbb{D}^*$ and annulus $\mathbb{A}(R)$ admit uniquely-determined complete hyperbolic metrics. Notice that both $\mathbb{D}^*$ and $\mathbb{A}(R)$ are homeomorphic with (open) cylinders. Due to this fact, the hyperbolic punctured disk $\mathbb{D}^*$ is also called the *parabolic cylinder* while the hyperbolic annuli $\mathbb{A}(R)$ are also called *hyperbolic cylinders* [8]. Summarizing, the list of elementary hyperbolic surfaces is as follows:

1. The hyperbolic disk $\mathbb{D}$ (which is isometric with the Poincaré half-plane $\mathbb{H}$).
2. The hyperbolic punctured disk $\mathbb{D}^*$ (uniformized to $\mathbb{H}$ by a parabolic cyclic subgroup of $\mathrm{PSL}(2, \mathbb{R})$).
3. The annuli $\mathbb{A}(R)$ for $R > 1$ (uniformized to $\mathbb{H}$ by a hyperbolic cyclic subgroup of $\mathrm{PSL}(2, \mathbb{R})$).

The explicit form of the hyperbolic metric is known in all cases, as is a fundamental polygon [13–15] for $\mathbb{D}^*$ and $\mathbb{A}(R)$. This allows one to study the cosmological dynamics of α-attractor

[2] A regular domain $\mathcal{D} \subset \mathbb{C}$ is called *doubly-connected* if its complement in the Riemann sphere has two connected components, which happens iff $\pi_1(\mathcal{D}) \simeq \mathbb{Z}$.

models defined by such surfaces either directly on (Σ, G) or (as explained in [1]) by lifting to the hyperbolic disk or to the Poincaré half-plane.

For elementary hyperbolic surfaces, the isometry classification of the ends is as follows [1, 8, 16]:

- The hyperbolic disk $\mathbb{D}$ has a single end, known as a *plane end*.
- The hyperbolic punctured disk $\mathbb{D}^*$ has two ends. One of these is a *cusp end*, the other being a *horn end*.
- The hyperbolic annulus $\mathbb{A}(R)$ has two ends, both of which are *funnel ends*.

All elementary hyperbolic surfaces are planar (i.e. of genus zero). As explained in [1], this implies that their end compactification [10, 11] is the unit sphere S^2. On the other hand, the conformal boundary $\partial^G_\infty \Sigma$ [1, 17, 18] differs in the three cases:

- For the hyperbolic disk, we have $\partial_\infty \mathbb{D} = \mathrm{S}^1$, where the circle corresponds to the plane end.
- For the hyperbolic punctured disk, we have $\partial_\infty \mathbb{D} = \{0\} \sqcup \mathrm{S}^1$, where the origin corresponds to the cusp end and S^1 corresponds to the horn end.
- For the hyperbolic annulus, we have $\partial_\infty \mathbb{A}(\mathbb{R}) = \mathrm{S}^1 \sqcup \mathrm{S}^1$, each of the circles corresponding to a funnel end.

Remark. By a theorem of Hilbert, a complete hyperbolic surface cannot be embedded isometrically into Euclidean 3-space. However, incomplete regions of such a surface can be embedded isometrically (and we shall see examples of such partial embeddings in latter sections). Notice that one can sometimes find isometric embeddings of complete hyperbolic surfaces into *non-Euclidean* three-space, such as the well-known embedding of the Poincaré disk as a sheet of a hyperboloid defined inside three-dimensional Minkowski space.

4 The hyperbolic disk

The cosmological model defined by the hyperbolic disk $\mathbb{D}$ coincides with the two-field α-attractor model of [7], which was discussed extensively in the literature. The purpose of this section is to show how this fits into the general theory developed in [1].

4.1 Semi-geodesic coordinates

The unit disk $\mathbb{D} = \{u \in \mathbb{C} \,|\, |u| < 1\}$ admits a unique complete hyperbolic metric, which is given by:

$$\mathrm{d}s^2_{\mathbb{D}} = |\lambda_{\mathbb{D}}(u, \bar{u})|^2 |\mathrm{d}u|^2 \quad , \text{ where } \quad \lambda_{\mathbb{D}}(u, \bar{u}) = \frac{2}{1 - |u|^2} \quad . \tag{4.1}$$

In polar coordinates given by $\rho = |u| \in (0, 1)$ and $\theta = \arg(u) \in (0, 2\pi)$, the metric becomes:

$$\mathrm{d}s^2_{\mathbb{D}} = \frac{4}{(1 - \rho^2)^2} \left(\mathrm{d}\rho^2 + \rho^2 \mathrm{d}\theta^2 \right) \quad .$$

Semi-geodesic coordinates (r, θ) for $\mathbb{D}$ are obtained by the change of variables:

$$\rho \stackrel{\text{def.}}{=} \tanh\left(\frac{r}{2}\right) \in (0,1) \;\; \text{i.e.} \;\; r = 2\,\text{arctanh}(\rho) = \log\frac{1+\rho}{1-\rho} \in (0,+\infty) \;\; .$$

This maps the unit disk (diffeomorphically, but not conformally) to the complex plane with polar coordinates (r, θ) and complex coordinate:

$$\zeta = re^{\mathbf{i}\theta} = 2\,\text{arctanh}(\rho)e^{\mathbf{i}\theta}$$

and brings the metric to the form:

$$\mathrm{d}s^2_{\mathbb{D}} = \mathrm{d}r^2 + \sinh^2(r)\mathrm{d}\theta^2 \;\; . \tag{4.2}$$

The single end of $\mathbb{D}$ (which is called a *plane end*) corresponds to $r \to +\infty$, while the center of $\mathbb{D}$ corresponds to $r \to 0$. The entire disk $\mathbb{D}$ is viewed as the canonical neighborhood of the end.

4.2 The end compactification of $\mathbb{D}$

The end compactification $\hat{\mathbb{D}}$ of the hyperbolic disk coincides with the Alexandroff compactification of the ζ-plane, which by the stereographic projection (2.8) is identified with the unit sphere S^2. The north pole $\psi = 0$ corresponds to the plane end at $r = |\zeta| \to \infty$, while the south pole $\psi = \pi$ corresponds to $r = 0$, i.e. to the center of $\mathbb{D}$. In spherical stereographic coordinates (ψ, θ), the Poincaré metric (4.2) becomes:

$$\mathrm{d}s^2_{\mathbb{D}} = \frac{1}{4}\frac{\mathrm{d}\psi^2}{\sin^2(\frac{\psi}{2})} + \sinh^2(\cot(\frac{\psi}{2}))\mathrm{d}\theta^2 \;\; .$$

Remark. The compact Riemann surface into which $\mathbb{D} = \{u \in \mathbb{C} \,|\, |u| < 1\}$ embeds holomorphically [17, 18] is the Riemann sphere $\mathbb{CP}^1$ associated to the u-plane. The coordinate u is given by:

$$u \stackrel{\text{def.}}{=} \frac{u_1}{u_2} \;\; \text{for} \;\; u_2 \neq 0 \;\; ,$$

where $(u_1, u_2) \in \mathbb{C}^2 \setminus \{0,0\}$ are the homogeneous coordinates of $\mathbb{CP}^1$.

4.3 Globally well-behaved scalar potentials on $\mathbb{D}$

A potential $\Phi : \mathbb{D} \to \mathbb{R}$ is globally well-behaved on $\mathbb{D}$ iff there exists a smooth function $\hat{\Phi} : \mathrm{S}^2 \to \mathbb{R}$ such that:

$$\Phi(r,\theta) = \hat{\Phi}(2\,\text{arccot}(r), \theta) \;\; , \tag{4.3}$$

i.e.:

$$\Phi(\rho,\theta) = \hat{\Phi}(2\,\text{arccot}(2\,\text{arctanh}\,\rho), \theta) \;\; .$$

The condition that $\hat{\Phi}$ is smooth on S^2 implies, in particular, that $\hat{\Phi}(\psi, \theta)$ has a finite limit for $\psi \to 0$ and hence $\Phi(r, \theta)$ has a θ-independent limit for $r \to +\infty$ i.e. for $|u| \to 1$. Expansion (2.3) gives the uniformly-convergent series:

$$\Phi(\rho,\theta) = \sum_{l=0}^{\infty}\sum_{m=-l}^{l} D_{lm}Y_{lm}(2\,\text{arccot}(2\,\text{arctanh}\,\rho), \theta) \;\; .$$

To obtain inflationary behavior with the scalar field rolling from the plane end towards the interior of $\mathbb{D}$, one can require that $\hat{\Phi}$ has a local maximum at the north pole of S^2. In the simplest models, one can take $\hat{\Phi}$ to have only two critical points, namely a global maximum at the north pole and a global minimum at the south pole. In that case, Φ has a global minimum at $u = 0$ (the center of $\mathbb{D}$) and increases monotonically to a θ-independent finite value as $|u|$ grows from zero to 1 (toward the conformal boundary $\partial_\infty \mathbb{D} = S^1$ of $\mathbb{D}$).

In polar coordinates (ρ, θ), the extended potentials (2.5) of Section 2 correspond to the following globally well-behaved scalar potentials on $\mathbb{D}$:

$$\Phi_+ = M_0 \frac{r^2}{1+r^2} = M_0 \frac{\left(\log \frac{1+\rho}{1-\rho}\right)^2}{1+\left(\log \frac{1+\rho}{1-\rho}\right)^2} \quad , \quad \Phi_- = \frac{M_0}{1+r^2} = \frac{M_0}{1+\left(\log \frac{1+\rho}{1-\rho}\right)^2} \quad , \tag{4.4}$$

where $\rho = |u|$. These potentials are shown in Figures 2a and 2b, which illustrate the characteristic stretching toward the end when the potential is expressed in semi-geodesic coordinates (r, θ) (with respect to which the two locally-defined real scalar fields of the sigma model have canonical kinetic terms). The supremum of Φ_+ corresponds to $\rho \to 1$ (being equal to M_0), while the infimum is attained at $\rho = 0$ (where Φ_+ vanishes). On the other hand, Φ_- tends to its vanishing infimum for $\rho \to 1$ and has a maximum at $\rho = 0$ (where it equals M_0). Notice that only Φ_+ leads to standard α-attractor behavior.

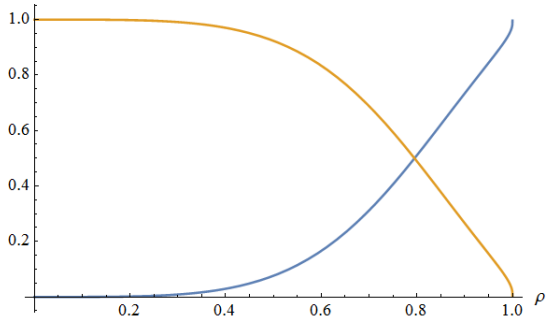

(a) Plot of Φ_+/M_0 (blue) and Φ_-/M_0 (yellow) as functions of $\rho \in [0, 1)$. The value $\rho = 0$ corresponds to the center of $\mathbb{D}$, while $\rho = 1$ corresponds to the conformal boundary $\partial_\infty \mathbb{D}$. Only the potential Φ_+ leads to α-attractor behavior when inflation takes place near the plane end.

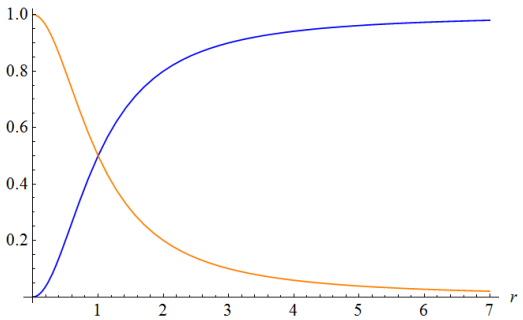

(b) Plot of Φ_+/M_0 (blue) and Φ_-/M_0 (yellow) as functions of $r \in [0, +\infty)$. The value $r = 0$ corresponds to the center of $\mathbb{D}$, while $r = +\infty$ corresponds to the plane end. Only the potential Φ_+ leads to α-attractor behavior when inflation takes place near the plane end.

Figure 2: The potentials $\Phi_\pm$ on the Poincaré disk.

Using the relation $\sin\psi = 2\sin(\psi/2)\cos(\psi/2) = \frac{2r}{1+r^2}$, the choice (2.6) gives the following potential on $\mathbb{D}$:

$$\Phi_0 = M_0 \left[1 + \frac{2r}{1+r^2}\cos\theta\right] = M_0 \left[1 + \frac{2\log\frac{1+\rho}{1-\rho}}{1+\left(\log\frac{1+\rho}{1-\rho}\right)^2}\cos\theta\right] \quad .$$

5 The hyperbolic punctured disk

The hyperbolic punctured disk $\mathbb{D}^*$ (also known as the "parabolic cylinder" [8]) is the simplest example of a hyperbolic surface with a cusp end. It also has a horn end.

5.1 The hyperbolic metric

The punctured unit disk $\mathbb{D}^* = \{u \in \mathbb{C} \,|\, 0 < |u| < 1\}$ admits a unique complete hyperbolic metric given by [19]:

$$\mathrm{d}s^2_{\mathbb{D}^*} = \lambda^2_{\mathbb{D}^*}(u,\bar{u})|\mathrm{d}u|^2 \quad , \text{ where } \quad \lambda_{\mathbb{D}^*}(u,\bar{u}) = \frac{1}{|u|\log(1/|u|)} \quad . \tag{5.1}$$

In particular, Reu and Imu are isothermal coordinates. In polar coordinates (ρ,θ) defined through:

$$u = \rho e^{\mathbf{i}\theta} \quad (\rho = |u| \in (0,1)) \quad ,$$

the metric takes the form:

$$\mathrm{d}s^2_{\mathbb{D}^*} = \frac{1}{(\rho\log\rho)^2}(\mathrm{d}\rho^2 + \rho^2\mathrm{d}\theta^2) \quad .$$

The center of $\mathbb{D}$ corresponds to the cusp end, while the bounding circle of $\mathbb{D}$ corresponds to the horn end (see below). The Euclidean circle at $\rho = e^{-2\pi}$ is a horocycle of length 1. Notice that $\mathbb{D}^*$ has infinite hyperbolic area.

5.2 Diffeomorphism to the punctured plane

One can introduce an orthogonal coordinate system $(\mathfrak{r},\theta) \in (0,+\infty)\times(0,2\pi)$ on $\mathbb{D}^*$ through the coordinate transformation:

$$\mathfrak{r} \stackrel{\text{def.}}{=} \frac{1}{\log\left(\frac{1}{\rho}\right)} = \frac{1}{|\log\rho|} \in (0,+\infty) \quad \text{i.e.} \quad \rho = e^{-\frac{1}{\mathfrak{r}}} \in (0,1) \quad . \tag{5.2}$$

This gives a diffeomorphism between $\mathbb{D}^*$ and the punctured complex plane $\mathbb{C}^* \stackrel{\text{def.}}{=} \mathbb{C}\setminus\{0\}$ with complex coordinate:

$$\zeta = \mathfrak{r}e^{\mathbf{i}\theta} \quad .$$

In this coordinate system, the metric (5.1) takes the form:

$$\mathrm{d}s^2_{\mathbb{D}^*} = \frac{1}{\mathfrak{r}^2}\mathrm{d}\mathfrak{r}^2 + \mathfrak{r}^2\mathrm{d}\theta^2 \quad . \tag{5.3}$$

The center of $\mathbb{D}^*$ corresponds to $\mathfrak{r} \to 0$, while the bounding circle of $\mathbb{D}^*$ corresponds to $\mathfrak{r} \to +\infty$.

5.3 Partial isometric embedding into Euclidean 3-space

One can isometrically embed the portion $0 < |u| < \frac{1}{e}$ of the hyperbolic punctured disk into Euclidean $\mathbb{R}^3$ as the open half-tractricoid[3] $\mathcal{E}$ defined in cylindrical coordinates $(\mathfrak{r}, \theta, x_3)$ (where $x_1 = \mathfrak{r}\cos\theta$ and $x_2 = \mathfrak{r}\sin\theta$) by the parametric equations:

$$\mathfrak{r} = \frac{1}{\cosh(\mathfrak{t})} \in (0,1) \quad , \quad x_3 = \mathfrak{t} - \tanh(\mathfrak{t}) \quad (\mathfrak{t} \in (0, +\infty)) \quad .$$

Indeed, it is easy to see that the Euclidean metric of $\mathbb{R}^3$ induces a metric on $\mathcal{E}$ which coincides with (5.3). This is the classical pseudosphere model of Beltrami (see Figure 3).

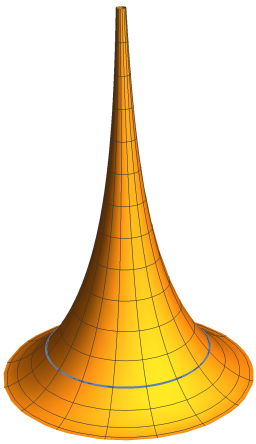

Figure 3: Upper half of a tractricoid (pseudosphere). The horocycle of length one is drawn in light blue. It separates the half-tractricoid into a cusp (upper part) and a portion of a horn (lower part). The latter is bounded by a horocycle of length 2π.

5.4 The end compactification of $\mathbb{D}^*$

The stereographic projection (2.8) identifies S^2 with the one-point compactification of the ζ-plane. This shows explicitly that S^2 is the end compactification of $\mathbb{D}^*$, where the north pole $\psi = 0$ corresponds to the horn end and the south pole $\psi = \pi$ corresponds to the cusp end. The embedding $j : \mathbb{D}^* \to \mathrm{S}^2$ is given by:

$$\psi = 2\arctan(|\log\rho|) \quad , \quad \theta = \theta \quad .$$

5.5 Semi-geodesic coordinates

The further change of variables:

$$\mathfrak{r} = \frac{1}{2\pi} e^{-r} \quad \text{i.e.} \quad r = -\log(2\pi\mathfrak{r}) = \log\left(\frac{|\log\rho|}{2\pi}\right) \in (-\infty, +\infty) \tag{5.4}$$

[3]The surface obtained by revolving an open half of a tractrix along its asymptote [20].

brings the metric (5.3) to the form:

$$\mathrm{d}s^2_{\mathbb{D}^*} = \mathrm{d}r^2 + \frac{e^{-2r}}{(2\pi)^2}\mathrm{d}\theta^2 \quad , \tag{5.5}$$

where $r \in \mathbb{R}$. In particular, (r, θ) are semi-geodesic coordinates. The center $u = 0$ of $\mathbb{D}^*$ corresponds to $r \to +\infty$ while the bounding circle $|u| = 1$ of $\mathbb{D}^*$ corresponds to $r \to -\infty$. The horocycle at $r = 0$ (i.e. $\rho = e^{-2\pi}$) has length 1.

5.6 The hyperbolic cusp

Let:

$$\kappa \stackrel{\text{def.}}{=} e^{-2\pi} \quad . \tag{5.6}$$

As mentioned above, the Euclidean circle $|u| = \kappa$ has hyperbolic length 1. The *hyperbolic cusp* (cf. [1]) corresponds to the portion of $\mathbb{D}^*$ lying inside this circle (see Figure 3), which is the open punctured disk:

$$\mathrm{C} \stackrel{\text{def.}}{=} \{u \in \mathbb{C} \mid 0 < |u| < \kappa\} \subset \mathbb{D}^* \quad , \tag{5.7}$$

endowed with the restriction of the metric (5.1); notice that the restricted metric is not complete. In coordinates $(\mathfrak{r}, \theta)$, the metric on C is obtained by restricting (5.3) to the range $\mathfrak{r} \in (0, \mathfrak{r}_0)$, where:

$$\mathfrak{r}_0 \stackrel{\text{def.}}{=} \frac{1}{2\pi} \quad .$$

In semi-geodesic coordinates (r, θ) the cusp metric is given by (5.5) with the restriction $r \in (0, +\infty)$. Notice that C has hyperbolic area equal to 1.

5.7 The hyperbolic horn

By definition, the *hyperbolic horn* is the annulus:

$$\mathrm{H} = \{u \in \mathbb{C} \mid \kappa < |u| < 1\} \subset \mathbb{D}^* \quad ,$$

endowed with the (incomplete) restriction of the metric (5.1). In coordinates $(\mathfrak{r}, \theta)$, the horn metric is obtained from (5.3) by restricting the range of $\mathfrak{r}$ to $(\mathfrak{r}_0, +\infty)$. In coordinates (r, θ), the metric takes the form (5.5), with the restriction $r \in (-\infty, 0)$. Defining $r' \stackrel{\text{def.}}{=} -r$, this can be brought to the form:

$$\mathrm{d}s^2_{\mathrm{H}} = (\mathrm{d}r')^2 + \frac{e^{2r'}}{(2\pi)^2}\mathrm{d}\theta^2 \quad , \quad \text{with} \quad r' \in (0, +\infty) \quad , \tag{5.8}$$

where the bounding circle $|u| = 1$ of $\mathbb{D}^*$ corresponds to $r' \to +\infty$.

5.8 Canonical uniformization to $\mathbb{H}$

The punctured disk is uniformized to the Poincaré half-plane (0.1) with complex coordinate τ by the parabolic cyclic group $\Gamma_P \stackrel{\text{def.}}{=} \langle P \rangle \subset \mathrm{PSL}(2, \mathbb{R})$ generated by the translation:

$$\tau \to \tau + 1 \quad , \tag{5.9}$$

which corresponds to the parabolic element:

$$P \stackrel{\text{def.}}{=} \begin{bmatrix} 1 & 1 \\ 0 & 1 \end{bmatrix} \in \mathrm{PSL}(2,\mathbb{R}) \quad . \tag{5.10}$$

This fixes the point $\tau = \infty \in \partial_\infty \mathbb{H}$. The holomorphic covering map is:

$$u = \pi_{\mathbb{H}}(\tau) = e^{2\pi \mathbf{i} \tau} \quad . \tag{5.11}$$

The hyperbolic cusp C is the projection through $\pi_{\mathbb{H}}$ of the cusp domain:

$$\mathcal{C}_{\mathbb{H}} = \{\tau \in \mathbb{H} | \mathrm{Im}\tau > 1\} \quad ,$$

which is bounded by the horocycle:

$$c_{\mathbb{H}} = \{\tau \in \mathbb{H} | \mathrm{Im}\tau = 1\} \quad .$$

This horocycle is tangent to the conformal boundary of $\mathbb{H}$ at the point $\tau = \infty$, which projects through $\pi_{\mathbb{H}}$ to the cusp ideal point of the end compactification of $\mathbb{D}^*$.

A fundamental polygon for the action of Γ_P on $\mathbb{H}$ is given by the semi-infinite vertical strip:

$$\mathfrak{D}_{\mathbb{H}} = \{\tau \in \mathbb{H} \,|\, 0 < \mathrm{Re}\tau < 1\} \quad , \tag{5.12}$$

and has vertices at the points (see Figure 4a):

$$A : \{\tau = \infty\} \ , \ B : \{\tau = 0\} \ , \ C : \{\tau = 1\} \quad . \tag{5.13}$$

The Poincaré side pairing maps (AB) into (AC) through the transformation (5.9), which generates Γ_P. The relative cusp neighborhood [1] with respect to $\mathfrak{D}_{\mathbb{H}}$ is the intersection $\mathfrak{C}_{\mathbb{H}} \stackrel{\text{def.}}{=} \mathcal{C}_{\mathbb{H}} \cap \mathfrak{D}_{\mathbb{H}}$. A lifted scalar potential $\tilde{\Phi} = \Phi \circ \pi_{\mathbb{H}}$ is given by:

$$\tilde{\Phi}(\tau) = \Phi(e^{2\pi i \tau}) \quad ,$$

being invariant under the translation (5.9). In particular, the restrictions of $\tilde{\Phi}$ to the sides (AB) and (AC) agree through the Poincaré pairing.

5.9 Canonical uniformization to $\mathbb{D}$

For completeness and comparison with [1], we also give the canonical uniformization of $\mathbb{D}^*$ to the hyperbolic disk. The Cayley transformation:

$$u = \frac{\mathbf{i} - \tau}{\mathbf{i}\tau - 1} \tag{5.14}$$

is an isometry from $\mathbb{H}$ to $\mathbb{D}$. When uniformizing $\mathbb{D}^*$ to $\mathbb{D}$, the fundamental polygon $\mathfrak{D}_{\mathbb{H}}$ becomes a hyperbolic triangle $\mathfrak{D}_{\mathbb{D}}$ with vertices at the following points, which correspond respectively to the points A, B and C of (5.13) through the Cayley transformation:

$$A' : \{u = \mathbf{i}\} \ , \ B' : \{u = -\mathbf{i}\} \ , \quad C' : \{u = 1\}$$

and a free side connecting the points B' and C' (see Figure 4b). The sides of this triangle are a segment connecting A' to B' (which passes through the origin of $\mathbb{D}$), the portion of $\partial_\infty\mathbb{D}$ connecting B' to C' and a Euclidean circular arc orthogonal to $\partial_\infty\mathbb{D}$ which connects A' to C'. The hyperbolic cusp neighborhood $\mathcal{C}_\mathbb{D}$ of the vertex A' is bounded by the horocycle:

$$c_\mathbb{D} = \left\{ \frac{t}{2 - \mathbf{i}t} \in \mathfrak{D}_\mathbb{D} \,|\, t \in \mathbb{R} \right\} \quad ,$$

which is tangent to $\partial_\infty\mathbb{D}$ at the point A'. The intersection of $\mathcal{C}_\mathbb{D}$ with $\mathfrak{D}_\mathbb{D}$ is the relative cusp neighborhood $\mathfrak{C}_\mathbb{D}$ with respect to $\mathfrak{D}_\mathbb{D}$ (see [1]), which is the image of $\mathfrak{C}_\mathbb{H}$ through the Cayley transformation.

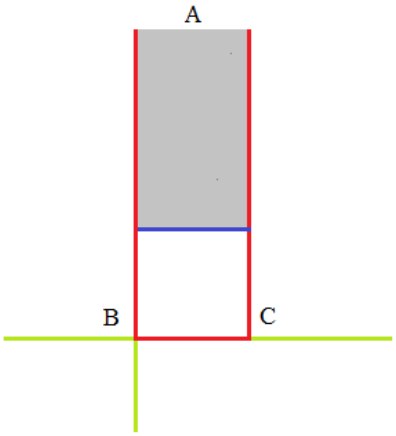

(a) A fundamental polygon $\mathfrak{D}_\mathbb{H}$ for the punctured disk on $\mathbb{H}$. The relative cusp neighborhood $\mathfrak{C}_\mathbb{H}$ of the vertex A corresponds to the shaded region.

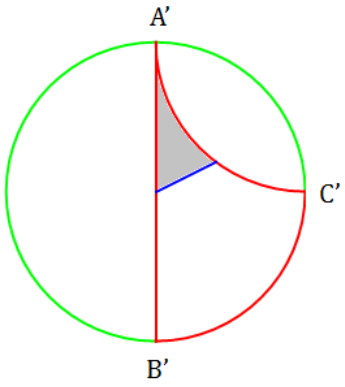

(b) A fundamental polygon $\mathfrak{D}_\mathbb{D}$ for the punctured disk on $\mathbb{D}$. The shaded region is the relative cusp neighborhood $\mathfrak{C}_\mathbb{D}$ of the vertex A'.

Figure 4: Fundamental polygons for the uniformization of $\mathbb{D}^*$ to the Poincaré half-plane and to the hyperbolic disk.

5.10 Globally well-behaved scalar potentials on $\mathbb{D}^*$

A scalar potential $\Phi : \Sigma \to \mathbb{R}$ is globally well-behaved on $\mathbb{D}^*$ iff there exists a smooth map $\hat{\Phi} : \mathrm{S}^2 \to \mathbb{R}$ such that:

$$\Phi(\mathfrak{r}, \theta) = \hat{\Phi}(2\,\mathrm{arccot}(\mathfrak{r}), \theta) \quad ,$$

i.e.:

$$\Phi(\rho, \theta) = \hat{\Phi}(2\arctan(|\log\rho|), \theta) \quad ,$$

where $\rho = |u|$. Expansion (2.3) gives the uniformly-convergent series:

$$\Phi(\rho, \theta) = \sum_{l=0}^{\infty} \sum_{m=-l}^{l} D_{lm} Y_{lm}(2\arctan(|\log\rho|), \theta) \quad .$$

For the choices (2.5) and (2.6), we find:

$$\begin{aligned}
\Phi_+ &= M_0 \frac{\mathfrak{r}^2}{1+\mathfrak{r}^2} = M_0 \frac{1}{1+(\log\rho)^2} \\
\Phi_- &= M_0 \frac{1}{1+\mathfrak{r}^2} = M_0 \frac{(\log\rho)^2}{1+(\log\rho)^2} \\
\Phi_0 &= M_0 \left[1 + \frac{2\mathfrak{r}\cos\theta}{1+\mathfrak{r}^2}\right] = M_0 \left[1 + \frac{2|\log\rho|}{1+(\log\rho)^2}\cos\theta\right] \quad .
\end{aligned} \tag{5.15}$$

These potentials are shown in Figure 5. Notice that Φ_+ leads to α-attractor behavior if inflation takes place near the horn end, while Φ_- leads to α-attractor behavior if inflation takes place near the cusp end [1]. The extended potentials $\hat{\Phi}_\pm$ have maxima and minima at the two ideal points of the end compactification of $\mathbb{D}^*$ (which correspond to the north and south poles of S^2). On the other hand, $\hat{\Phi}_0$ does *not* have extrema at the ideal points; its extrema coincide with those of Φ_0, being located inside $\mathbb{D}^*$. The minimum (equal to zero) is at the point $u = -\frac{1}{e} \approx -0.36$ while the maximum (equal to $2M_0$) is at $u = +\frac{1}{e} \approx +0.36$.

Remark. Using (5.4), we find the following expressions in semi-geodesic coordinates:

$$\Phi_+(r) = \frac{M_0}{1+(2\pi)^2 e^{2r}} \ , \ \Phi_-(r) = \frac{M_0}{1+\frac{e^{-2r}}{(2\pi)^2}} \ , \ \Phi_0(r,\theta) = M_0\left[1 + \frac{4\pi e^{-r}\cos\theta}{(2\pi)^2 + e^{-2r}}\right] \quad . \tag{5.16}$$

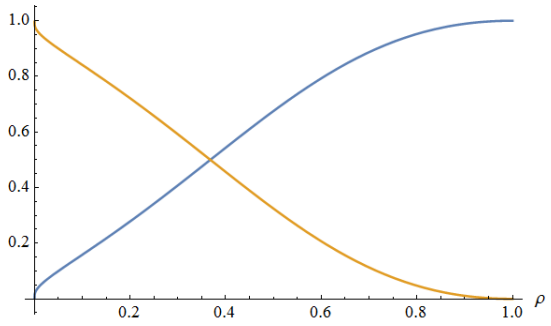

(a) Plot of Φ_+/M_0 (blue) and Φ_-/M_0 (yellow) as functions of $\rho \in (0,1)$. The value $\rho = 0$ corresponds to the cusp end, while $\rho = 1$ corresponds to the horn end.

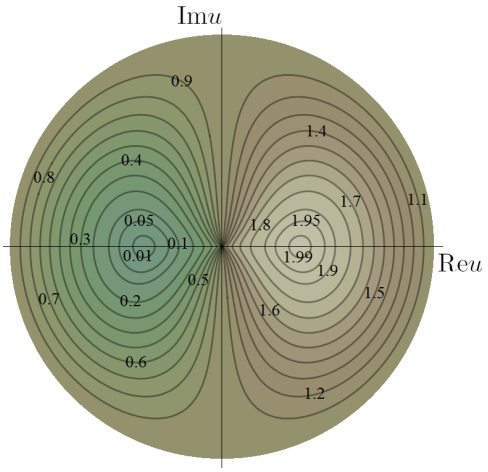

(b) Level plot of Φ_0/M_0 on the punctured disk. Darker tones indicate lower values of Φ_0/M_0.

Figure 5: The potentials $\Phi_\pm$ and Φ_0 on the hyperbolic punctured disk.

Lift of the potentials $\Phi_\pm$ and Φ_0 to $\mathbb{H}$. Consider the well-behaved scalar potentials $\Phi_\pm$ and Φ_0 on $\mathbb{D}^*$ given in (5.15). Let $x = \mathrm{Re}\tau$ and $y \stackrel{\text{def.}}{=} \mathrm{Im}\tau$. Then the covering map (5.11) reads:

$$u = \pi_{\mathbb{H}}(\tau) = e^{2\pi \mathbf{i}\tau} = e^{-2\pi y}[\cos(2\pi x) + \mathbf{i}\sin(2\pi x)] \quad ,$$

which gives:

$$\rho = |u| = e^{-2\pi y} \quad , \quad \theta = \arg(u) = 2\pi x \ (\mathrm{mod}\, 2\pi) \quad . \tag{5.17}$$

Hence the potentials $\Phi_\pm$ and Φ_0 have the following lifts to $\mathbb{H}$ (see Figure 6):

$$\tilde{\Phi}_+ = M_0 \frac{1}{1+(2\pi)^2 y^2} \quad , \quad \tilde{\Phi}_- = M_0 \frac{y^2}{(2\pi)^{-2}+y^2} \quad , \quad \tilde{\Phi}_0 = M_0 \left[1 + \frac{4\pi y \cos(2\pi x)}{1+4\pi^2 y^2}\right] \quad . \tag{5.18}$$

The function $\tilde{\Phi}_0(\tau)$ (which is periodic under $\tau \to \tau+1$) attains its minimum $\min \tilde{\Phi}_0 = 0$ at the points $\tau = n + \frac{1}{2} + \frac{\mathbf{i}}{2\pi} \approx n + 0.5 + 0.16\mathbf{i}$ (with $n \in \mathbb{Z}$), while the maximum $\max \tilde{\Phi}_0 = 2M_0$ is attained for $\tau = n + \frac{\mathbf{i}}{2\pi} \approx n + 0.16\mathbf{i}$ with $n \in \mathbb{Z}$.

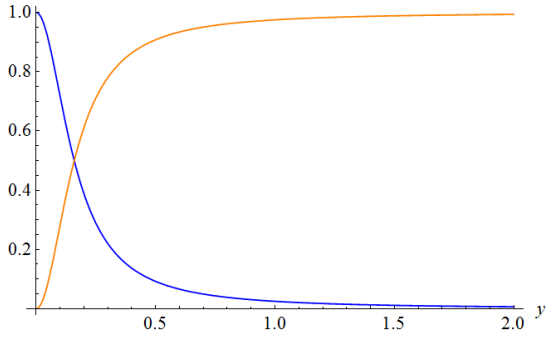

(a) Plot of $\tilde{\Phi}_+/M_0$ (blue) and $\tilde{\Phi}_-/M_0$ (yellow) as functions of $y = \mathrm{Im}\tau \in (0, +\infty)$. The values $y = 0$ and $y = +\infty$ correspond respectively to the horn and cusp ends.

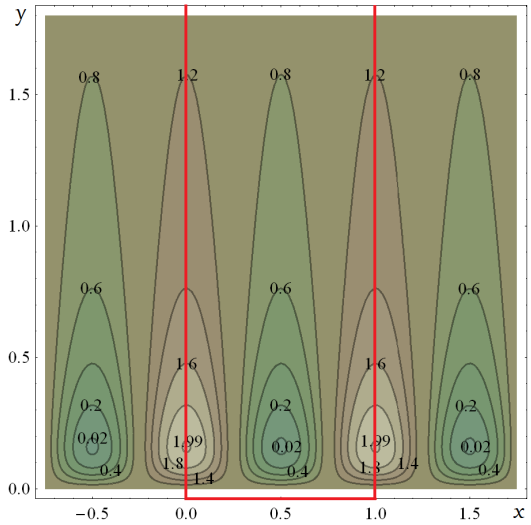

(b) Level sets of $\tilde{\Phi}_0/M_0$. Higher values of $\tilde{\Phi}_0$ correspond to lighter tones. The fundamental domain $\mathfrak{D}_\mathbb{H}$ is bounded by the red lines.

Figure 6: The lifted potentials $\tilde{\Phi}_\pm$ and $\tilde{\Phi}_0$.

5.11 Cosmological trajectories on the hyperbolic punctured disk

We now present examples of numerically-computed trajectories on $\mathbb{D}^*$ for the vanishing scalar potential and for the globally well-behaved scalar potentials $\Phi_\pm$ and Φ_0. These were obtained as explained in Subsection 1.2, by numerically computing solutions of the system (1.3) on the Poincaré half-plane for the corresponding lifted potentials and then projecting these trajectories to the hyperbolic punctured disk using the explicitly-known uniformization map (5.11) (which is equivalent with (5.17)).

Trajectories for vanishing scalar potential. To understand the effect of the hyperbolic metric on the dynamics, we start with the case of a vanishing scalar potential $\Phi = 0$. Then $\tilde{\Phi} = 0$ and one immediately checks that straight lines given by constant functions $x(t) = x_0, y(t) = y_0$ are solutions of (1.2) for any initial point $(x_0, y_0) \in \mathbb{H}$, with initial velocity zero. This means that a scalar field starting "at rest" remains at rest for all times.

On the other hand, numerical computation shows that any solution of (1.2) tends to the real axis for $t \to +\infty$, irrespective of its initial conditions. As a consequence, any solution defined on $\mathbb{D}^*$ (which is obtained by projecting a solution defined on $\mathbb{H}$ through the map (5.11)) will tend toward the horn end as $t \to +\infty$. This shows that the hyperbolic metric produces an effective force which attracts φ to that end. Notice that a global trajectory defined on $\mathbb{D}^*$ can have self-intersection points and hence it need not correspond to an embedded curve in $\mathbb{D}^*$.

Figure 7 shows a stationary trajectory and three other trajectories on $\mathbb{H}$ and their projections to $\mathbb{D}^*$ for $\Phi = 0$ and $\alpha = \frac{M_0}{3}$, with the following initial conditions:

trajectory	τ_0	$\tilde{v}_0$
orange	$0.3 + \mathbf{i}/(2\pi)$	0
red	$(1 + 2\mathbf{i})/10$	$2 + 3\mathbf{i}$
blue	$\mathbf{i}$	$1 + \mathbf{i}$
magenta	$\mathbf{i}/10$	$1.3 + 7\mathbf{i}$

Table 1: Initial conditions for four trajectories on the Poincaré half-plane.

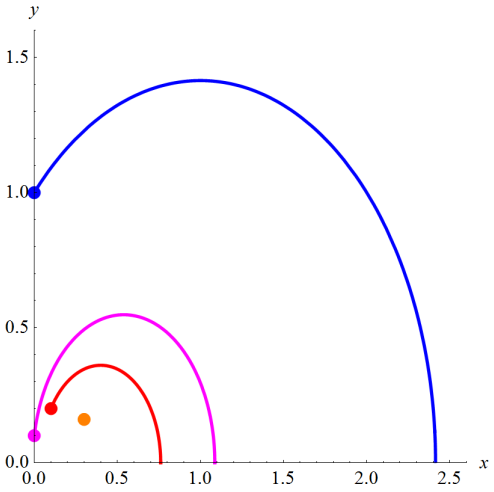

(a) Trajectories for $\Phi = 0$ on the Poincaré half-plane. The solution shown in orange is stationary.

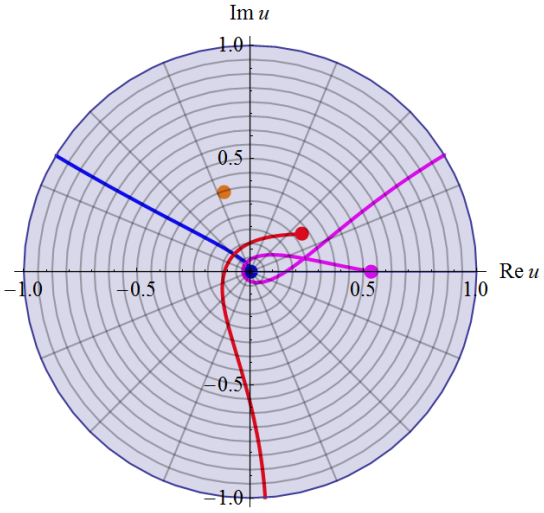

(b) Projection of the trajectories shown at the left to the hyperbolic punctured disk.

Figure 7: Numerical solutions for $\Phi = 0$ and $\alpha = \frac{M_0}{3}$.

Trajectories for Φ_-. Four lifted trajectories (and their projections to $\mathbb{D}^*$) for $\alpha = \frac{M_0}{3}$ and $\Phi = \Phi_-$ with the initial conditions given in Table 1 are shown in Figure 8. Since $\hat{\Phi}_-$ has a maximum at the cusp end (center of the disk) and a minimum at the horn end, it reinforces the effect of the hyperbolic metric, together with which it produces an effective attraction to the horn end. In particular, a trajectory which starts with vanishing initial

velocity is no longer stationary, but evolves for $t \to +\infty$ to the horn end (see the orange trajectory in the figures). Any other trajectory (irrespective of its initial velocity) also evolves for $t \to +\infty$ to the horn end.

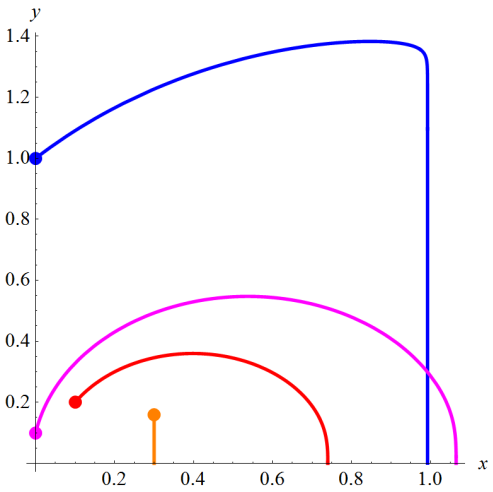

(a) Trajectories for $\Phi = \Phi_-$ on the Poincaré half-plane.

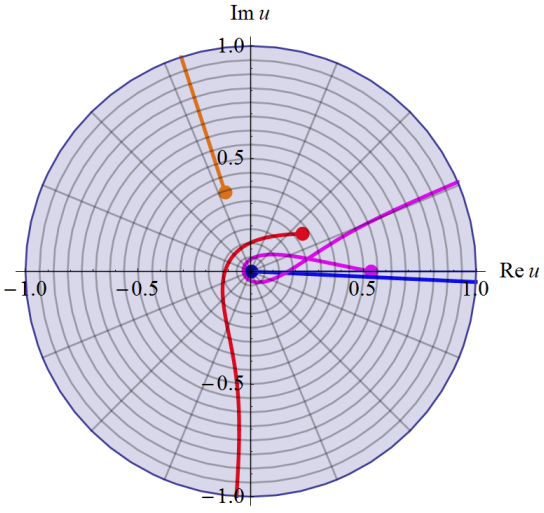

(b) Projection of the trajectories shown at the left to the hyperbolic punctured disk.

Figure 8: Numerical solutions for $\Phi = \Phi_-$ and $\alpha = \frac{M_0}{3}$.

Trajectories for Φ_+. Four lifted trajectories for $\alpha = \frac{M_0}{3}$ and $\Phi = \Phi_+$ (and their projections to $\mathbb{D}^*$) with the initial conditions given in Table 1 are shown in Figure 9. Since $\hat{\Phi}_+$ has a minimum at the cusp end (which corresponds to the center of the disk), it produces an attractive force towards the cusp end, which acts as a counterbalance to the effect of the hyperbolic metric.

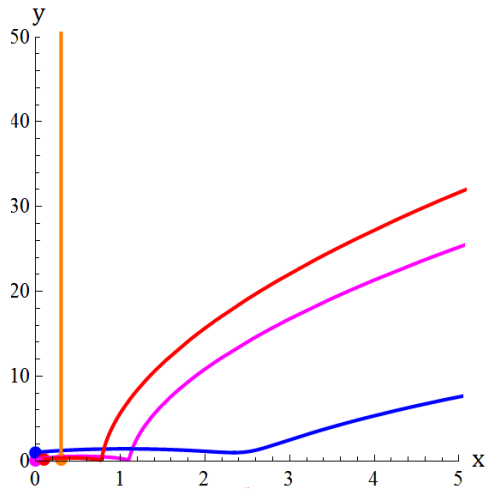

(a) Trajectories for $\Phi = \Phi_+$ on the Poincaré half-plane.

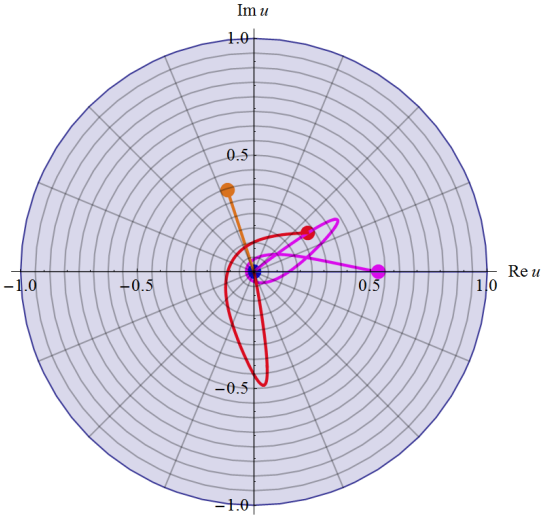

(b) Projection of the trajectories shown at the left to the hyperbolic punctured disk.

Figure 9: Numerical solutions for $\Phi = \Phi_+$ and $\alpha = \frac{M_0}{3}$.

Trajectories for Φ_0. Four lifted trajectories (and their projections to $\mathbb{D}^*$) for $\alpha = \frac{M_0}{3}$ and $\Phi = \Phi_0$ with the initial conditions given in Table 1 are shown in Figure 10.

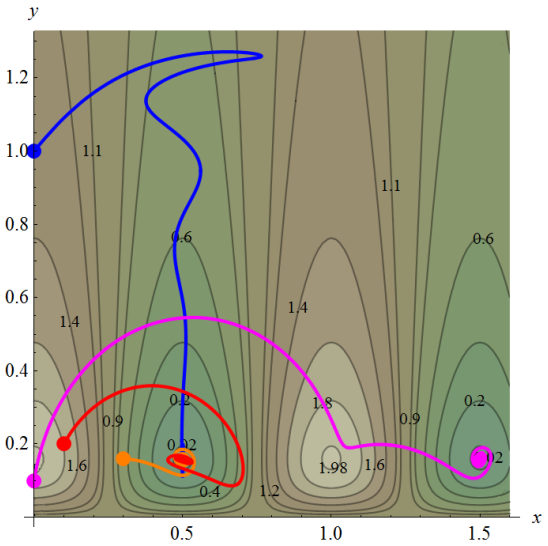

(a) Trajectories for $\Phi = \Phi_0$ on the Poincaré half-plane.

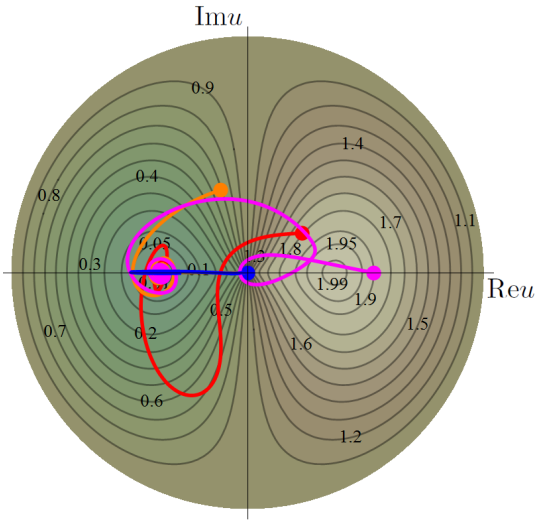

(b) Projection of the trajectories shown at the left to the hyperbolic punctured disk.

Figure 10: Numerical solutions for $\Phi = \Phi_0$ and $\alpha = \frac{M_0}{3}$.

Figure 11 shows in more detail the behavior of the magenta trajectory of Figure 10a near the local minimum of $\tilde{\Phi}_0$ located at $\tau = \frac{3}{2} + \frac{\mathbf{i}}{2\pi}$ (which projects to $u = -\frac{1}{e}$) and of its

projection to $\mathbb{D}^*$. For this solution, φ evolves in a spiral around the minimum of Φ_0, until it settles at the minimum.

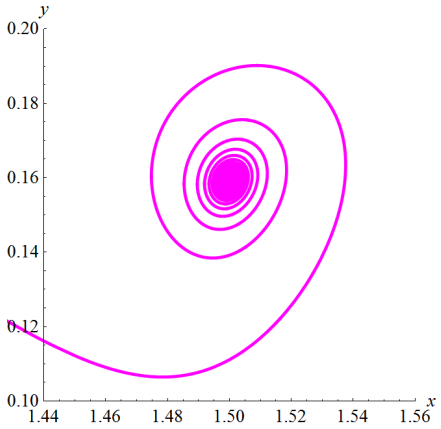

(a) Detail of the magenta trajectory shown in Figure 10a near the minimum of $\tilde{\Phi}_0$ located at $\tau = \frac{3}{2} + \frac{\mathbf{i}}{2\pi}$

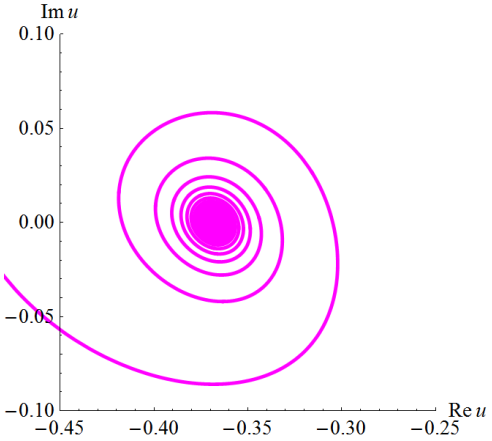

(b) Projection of the trajectory shown at the left to the hyperbolic punctured disk.

Figure 11: Detail of the magenta trajectory.

6 Hyperbolic annuli

Hyperbolic annuli (also known as "hyperbolic cylinders" [8]) have a single modulus and two funnel ends.

6.1 The hyperbolic metric

Let $R > 1$ be a real number. The annulus $\mathbb{A}(R) = \{u \in \mathbb{C} \,|\, \frac{1}{R} < |u| < R\}$ of modulus $\mu = 2\ln R > 0$ admits a unique complete hyperbolic metric, which is given by [19]:

$$\mathrm{d}s_R^2 = \lambda_R(u,\bar{u})^2 |\mathrm{d}u|^2 \quad , \text{ where } \quad \lambda_R(u,\bar{u}) = \frac{\pi}{2\log R} \frac{1}{|u| \cos\left(\frac{\pi \log|u|}{2\log R}\right)} \quad . \tag{6.1}$$

In particular, Reu and Imu are isothermal coordinates. Notice that the transformation $u \to \frac{1}{\bar{u}}$ is an isometry. In polar coordinates (ρ, θ) defined through:

$$u = \rho e^{\mathbf{i}\theta} \quad , \text{ with } \quad \rho = |u| \in (\frac{1}{R}, R) \quad ,$$

the metric takes the form:

$$\mathrm{d}s_R^2 = \left(\frac{\pi}{2\log R}\right)^2 \frac{\mathrm{d}\rho^2 + \rho^2 \mathrm{d}\theta^2}{\left[\rho \cos\left(\frac{\pi \log \rho}{2\log R}\right)\right]^2} \quad . \tag{6.2}$$

For any $\rho \in (1/R, R)$, the Euclidean circle $c_\rho \stackrel{\text{def.}}{=} \{u \in \mathbb{C} | |u| = \rho\}$ has hyperbolic circumference given by:

$$\ell_R(c_\rho) = \frac{\pi^2}{(\log R) \cos\left(\frac{\pi \log \rho}{2\log R}\right)} \quad .$$

We have:

$$\ell_R(c_\rho) = \ell_R(c_{1/\rho}) \quad .$$

Notice that $\ell_R(c_\rho)$ increases from $\frac{\pi^2}{\log R}$ to infinity as ρ increases from 1 to R and as ρ decreases from 1 to $1/R$. In particular, the minimum hyperbolic length is attained for the circle c_1 of Euclidean radius $\rho = 1$, which is the only closed hyperbolic geodesic of $\mathbb{A}(R)$ and has hyperbolic length:

$$\ell \stackrel{\text{def.}}{=} \ell_R(c_1) = \frac{\pi^2}{\log R} = \frac{2\pi^2}{\mu} \quad , \tag{6.3}$$

known as the *hyperbolic circumference* of $\mathbb{A}(R)$. The lines:

$$\{te^{i\theta} | t \in (1/R, R)\}$$

are geodesics of infinite length. Notice that the hyperbolic area of $\mathbb{A}(R)$ is infinite. Relation (6.3) gives:

$$R = R_\ell = e^{\frac{\pi^2}{\ell}} \quad . \tag{6.4}$$

6.2 Diffeomorphism to the punctured disk and to the punctured plane

The annulus $\mathbb{A}(R)$ is diffeomorphic (but not biholomorphic !) with the punctured unit disk with complex coordinate u' through the map:

$$u' = f(u) = \frac{|u| - \frac{1}{R}}{(R - \frac{1}{R})|u|} u \in \mathbb{D}^* \quad (u \in \mathbb{A}(R)) \quad , \tag{6.5}$$

whose inverse is given by:

$$u = f^{-1}(u') = \frac{(R - \frac{1}{R})|u'| + \frac{1}{R}}{|u'|} u' \in \mathbb{A}(R) \quad (u' \in \mathbb{D}^*) \quad .$$

Notice that f maps the Euclidean circle $|u| = \frac{1}{R}$ to $u' = 0$ and the Euclidean circle $|u| = R$ to the Euclidean circle $|u'| = 1$. Composing f with the map (5.2) gives a diffeomorphism from $\mathbb{A}(R)$ to the punctured complex plane with coordinate:

$$\zeta = \mathfrak{r} e^{\mathbf{i}\theta} \quad ,$$

where:

$$\mathfrak{r} = -\frac{1}{\log |u'|} = \frac{1}{\log \frac{R - \frac{1}{R}}{|u| - \frac{1}{R}}} = \frac{1}{\log \frac{R - \frac{1}{R}}{\rho - \frac{1}{R}}} \quad . \tag{6.6}$$

The funnel end at $|u| = \frac{1}{R}$ corresponds to $\zeta = 0$ while the funnel end at $|u| = R$ corresponds to $\zeta = \infty$.

6.3 The end compactification of $\mathbb{A}(R)$

The end compactification of $\mathbb{A}(R)$ is the unit sphere S^2 with polar coordinates $(\psi, \theta) \in (0, \pi) \times (0, 2\pi)$, which maps to the ζ-plane through the stereographic projection (2.8). The funnel end at $|u| = \frac{1}{R}$ corresponds to the south pole, while the funnel end at $|u| = R$ corresponds to the north pole. The explicit embedding of $\mathbb{A}(R)$ into S^2 is given by:

$$\psi = 2 \arctan \left(\log \frac{R - \frac{1}{R}}{\rho - \frac{1}{R}} \right) \quad , \quad \theta = \theta \quad .$$

6.4 The hyperbolic funnel

Let $\ell > 0$ be a positive real number and R_ℓ be defined as in (6.4). By definition, a *hyperbolic funnel* (cf. [1]) of circumference $\ell > 0$ is the annulus:

$$\mathrm{F}_\ell = \{u \in \mathbb{C} \mid \frac{1}{R_\ell} < |u| < 1\} \subset \mathbb{A}(R_\ell) \quad , \tag{6.7}$$

endowed with the restriction of the metric (6.1). Since $u \to \frac{1}{\bar{u}}$ is an isometry of $\mathbb{A}(R)$, the funnel is isometric with the annulus $1 < |u| < R_\ell$ (endowed with the restriction of (6.1)). Hence $\mathbb{A}(R)$ decomposes as the disjoint union of two funnels and the closed geodesic c_1. Notice that a funnel has infinite hyperbolic area. The funnel is diffeomorphic (but not conformally equivalent !) with the punctured unit disk through the map:

$$u' = \frac{|u| - \frac{1}{R_\ell}}{(1 - \frac{1}{R_\ell})|u|} u \in \mathbb{D}^* \quad (u \in \mathrm{F}_\ell) \quad , \tag{6.8}$$

which takes the funnel end $u \to \frac{1}{R_\ell}$ to the center $u' \to 0$ of the unit disk and the circle c_1 into the bounding circle of the unit disk.

6.5 Semi-geodesic coordinates on F_ℓ

Consider orthogonal coordinates (q, θ) on F_ℓ given by:

$$q = \frac{\pi}{\mu} \frac{1}{\cos(\frac{\pi}{\mu} \log \rho)} \in (\frac{\pi}{\mu}, +\infty) \quad ,$$

where $\rho = |u|$ and $\theta \in (0, 2\pi)$ is the polar angle in the u-plane. The limit $\rho \to 1/R$ corresponds to $q \to \infty$, while $\rho \to 1$ corresponds to $q \to \frac{\pi}{\mu} = \frac{\ell}{2\pi}$. In these coordinates, the metric on F_ℓ becomes:

$$\mathrm{d}s^2_{\mathrm{F}_\ell} = \frac{1}{q^2 - \left(\frac{\pi}{\mu}\right)^2} \mathrm{d}q^2 + q^2 \mathrm{d}\theta^2 = \frac{1}{q^2 - \left(\frac{\ell}{2\pi}\right)^2} \mathrm{d}q^2 + q^2 \mathrm{d}\theta^2 \quad . \tag{6.9}$$

The coordinates θ and:

$$r \stackrel{\text{def.}}{=} \operatorname{arccosh}\left(\frac{2\pi}{\ell} q\right) = \operatorname{arccosh}\left[\frac{1}{\cos(\frac{\pi}{\mu} \log \rho)}\right] \in (0, +\infty) \tag{6.10}$$

are semi-geodesic on F_ℓ. In these coordinates, the metric takes the form:

$$\mathrm{d}s^2_{\mathrm{F}_\ell} = \mathrm{d}r^2 + \frac{\ell^2}{(2\pi)^2} \cosh^2(r) \mathrm{d}\theta^2 \quad . \tag{6.11}$$

The limit $\rho \to 1/R$ corresponds to $r \to +\infty$ while $\rho \to 1$ corresponds to $r \to 0$. The parameter $\ell > 0$ is the hyperbolic length of the geodesic at $r = 0$.

6.6 Partial isometric embedding of the funnel into Euclidean 3-space

One can isometrically embed the annulus $\mathrm{F}_\ell^0 \subset \mathrm{F}_\ell$ corresponding to the range:

$$\frac{\ell}{2\pi} = \frac{\pi}{\mu} < q \leq \sqrt{1 + \left(\frac{\pi}{\mu}\right)^2} = \sqrt{1 + \left(\frac{\ell}{2\pi}\right)^2}$$

into Euclidean $\mathbb{R}^3$ as the surface of revolution defined by the parametric equations (see [20, Chap. 3C] or [21, Chap. 15]):

$$x_1 = q(r)\cos\theta \quad , \quad x_2 = q(r)\sin\theta \; , \quad x_3 = \xi(r) \quad , \text{ with } \quad r \in \left(0, \operatorname{arcsinh}\left(\frac{2\pi}{\ell}\right)\right) \quad ,$$

where:

$$\begin{aligned} q(r) \;&=\; \frac{\ell}{2\pi}\cosh(r) \in \left(\frac{\ell}{2\pi}, \sqrt{1 + \left(\frac{\ell}{2\pi}\right)^2}\right) \quad (\text{see} \;\; (6.10)) \\ \xi(r) \;&\stackrel{\text{def.}}{=}\; \int_0^r \mathrm{d}r' \sqrt{1 - \left(\frac{\ell}{2\pi}\right)^2 \sinh^2(r')} = -\mathbf{i}\,\mathrm{E}\left(\mathbf{i}r \,, -\left(\frac{\ell}{2\pi}\right)^2\right) \quad , \end{aligned}$$

and $\mathrm{E}(\tau, m)$ denotes the elliptic integral of the second kind. This is one of the three[4] types of (incomplete) classical surfaces of revolution in $\mathbb{R}^3$ of constant Gaussian curvature equal to -1, namely a surface of "hyperboloid type" (see Figure 12).

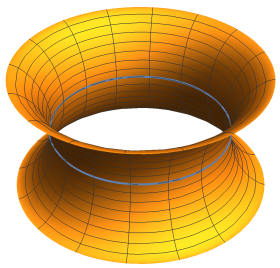

Figure 12: Hyperbolic surface of revolution of hyperboloid type. The upper half corresponds to the region F_ℓ^0 of F_ℓ. The circle drawn in light blue is the closed geodesic of length ℓ.

6.7 Canonical uniformization to $\mathbb{H}$

The hyperbolic annulus $\mathbb{A}(R_\ell)$ is uniformized to the upper half plane by the hyperbolic cyclic subgroup generated by the transformation:

$$\tau \to e^\ell \tau \quad , \tag{6.12}$$

[4]The other two are the pseudosphere/tractricoid (which corresponds to a portion of the hyperbolic cusp) and the surface of "conical type".

which corresponds to the hyperbolic element:

$$H_\ell \stackrel{\text{def.}}{=} \begin{bmatrix} e^{\ell/2} & 0 \\ 0 & e^{-\ell/2} \end{bmatrix} \in \mathrm{PSL}(2,\mathbb{R}) \tag{6.13}$$

and fixes the points $\tau = 0$ and $\tau = \infty$ lying on $\partial_\infty \mathbb{H}$. The holomorphic covering map is:

$$u = \pi_{\mathbb{H}}(\tau) = R_\ell e^{\frac{2\pi i}{\ell}\log\tau} = e^{\frac{\pi^2}{\ell} + \frac{2\pi i}{\ell}\log\tau} \quad , \tag{6.14}$$

which gives:

$$\rho = e^{\frac{\pi^2}{\ell} - \frac{2\pi}{\ell}\arg(\tau)} \quad , \quad \theta = \frac{2\pi}{\ell}\log|\tau| \pmod{2\pi} \quad . \tag{6.15}$$

A fundamental polygon is given by (see Figure 13a):

$$\mathfrak{D}_{\mathbb{H}} = \left\{ \tau \in \mathbb{H} \mid e^l < |\tau| < e^{2l} \right\} \quad . \tag{6.16}$$

This is a hyperbolic quadrilateral with two free sides and vertices located at the points:

$$A : \{\tau = -e^{2\ell}\} \ , \ B : \{\tau = -e^{\ell}\} \ , \ C : \{\tau = e^{\ell}\} \quad , \quad D : \{\tau = e^{2\ell}\} \quad . \tag{6.17}$$

The funnel F_ℓ is the projection of the relative funnel neighborhood [1]:

$$\mathfrak{F}^\ell_{\mathbb{H}} = \{\tau \in \mathfrak{D}_{\mathbb{H}} | \mathrm{Re}\tau < 0\} = \{\tau \in \mathfrak{D}_{\mathbb{H}} | \arg(\tau) \in \left(\frac{\pi}{2}, \pi\right)\} \quad .$$

6.8 Canonical uniformization to $\mathbb{D}$

When passing to the disk model, the fundamental domain $\mathfrak{D}_{\mathbb{H}}$ is mapped by the Cayley transformation (5.14) to a hyperbolic quadrilateral $\mathfrak{D}_{\mathbb{D}}$ with vertices located at the following points, which are obtained from the points A, B, C, D defined in (6.17) by applying (5.14):

$$A' : \{u = -\frac{\mathbf{i} + e^{2l}}{\mathbf{i}e^{2l} + 1}\} \quad , \quad B' : \{u = -\frac{\mathbf{i} + e^{l}}{\mathbf{i}e^{l} + 1}\} \quad , \quad C' : \{u = \frac{\mathbf{i} - e^{l}}{\mathbf{i}e^{l} - 1}\} \quad , \quad D' : u = \{\frac{\mathbf{i} - e^{2l}}{\mathbf{i}e^{2l} - 1}\} \quad .$$

The free sides $(A'B')$ and $(C'D')$ are portions of $\partial_\infty \mathbb{D}$ (see Figure 13b), while the sides $(B'C')$ and $(A'D')$ are arc segments of Euclidean circles which are orthogonal to $\partial_\infty \mathbb{D}$.

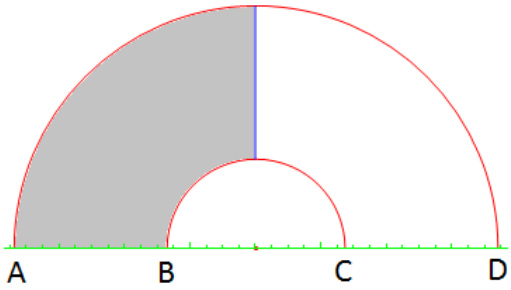

(a) Fundamental domain $\mathfrak{D}_{\mathbb{H}}$ for $\mathbb{A}(R)$ on the Poincaré half-plane. The shaded region is the relative funnel neighborhood $\mathfrak{F}_{\mathbb{H}}$ corresponding to the free side on the left.

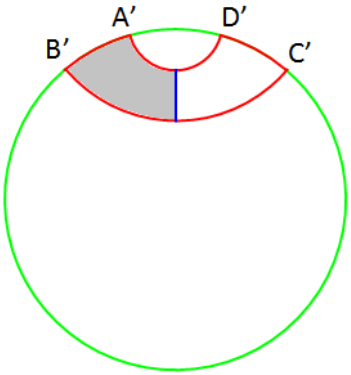

(b) Fundamental domain $\mathfrak{D}_{\mathbb{D}}$ for $\mathbb{A}(R)$ on the Poincaré disk. The shaded region is the relative funnel neighborhood of the free side on the left.

Figure 13: Fundamental domains for the uniformization of the hyperbolic annulus to the Poincaré half-plane and to the hyperbolic disk.

6.9 Globally well-behaved scalar potentials on $\mathbb{A}(R)$

A scalar potential Φ on $\mathbb{A}(R)$ is globally well-behaved iff there exists a smooth function $\hat{\Phi} : \mathrm{S}^2 \to \mathbb{R}$ such that:

$$\Phi(\mathfrak{r}, \theta) = \hat{\Phi}(2\,\mathrm{arccot}(\mathfrak{r}), \theta) \quad ,$$

i.e.:

$$\Phi(\rho, \theta) = \hat{\Phi}\left(2\arctan\left(\log\frac{R-\frac{1}{R}}{\rho-\frac{1}{R}}\right), \theta\right) \quad .$$

Expansion (2.3) gives the uniformly-convergent series:

$$\Phi(\rho, \theta) = \sum_{l=0}^{\infty}\sum_{m=-l}^{l} D_{lm} Y_{lm}\left(2\arctan\left(\log\frac{R-\frac{1}{R}}{\rho-\frac{1}{R}}\right), \theta\right) \quad .$$

For the choices (2.5), we find:

$$\Phi_+ = M_0\frac{\mathfrak{r}^2}{1+\mathfrak{r}^2} = M_0\frac{1}{1+\left[\log\frac{R-\frac{1}{R}}{\rho-\frac{1}{R}}\right]^2} \quad , \quad \Phi_- = M_0\frac{1}{1+\mathfrak{r}^2} = M_0\frac{\left[\log\frac{R-\frac{1}{R}}{\rho-\frac{1}{R}}\right]^2}{1+\left[\log\frac{R-\frac{1}{R}}{\rho-\frac{1}{R}}\right]^2} \quad , \quad (6.18)$$

where $\rho = |u| \in (\frac{1}{R}, R)$ and we used (6.6). The potentials $\Phi_\pm$ are plotted in Figure 14a for the case $\ell = \pi^2$ ($R = e$). For the choice (2.6), we find:

$$\Phi_0 = M_0\left[1 + \frac{2\mathfrak{r}}{1+\mathfrak{r}^2}\cos\theta\right] = M_0\left[1 + \frac{2\log\frac{R-\frac{1}{R}}{\rho-\frac{1}{R}}}{1+\left(\log\frac{R-\frac{1}{R}}{\rho-\frac{1}{R}}\right)^2}\cos\theta\right] \quad . \quad (6.19)$$

Recall that $\hat{\Phi}_0$ has two extrema on S^2, which are located at $(\psi, \theta) = (\frac{\pi}{2}, 0)$ (maximum) and $(\psi, \theta) = (\frac{\pi}{2}, \pi)$ (minimum). At each of these points, relation (2.8) gives $\mathfrak{r} = \cot(\frac{\pi}{4}) = 1$, so (6.6) gives $\rho = \rho_0$, where:

$$\rho_0 \stackrel{\text{def.}}{=} \frac{1}{R} + \frac{1}{e}(R - \frac{1}{R}) \quad . \tag{6.20}$$

It follows that the two critical points of Φ_0 on $\mathbb{A}(R)$ are located on the real axis at:

- $u_M = +\rho_0$, where Φ_0 attains its maximum (which equals $2M$)
- $u_m = -\rho_0$, where Φ_0 attains its minimum (which equals zero).

The level curves of Φ_0 are shown in Figure 14b for the case $\ell = \pi^2$ ($R = e$), which gives $\rho_0 = \frac{e^2+e-1}{e^2} = 1 + \frac{1}{e} - \frac{1}{e^2} \approx 1.23$.

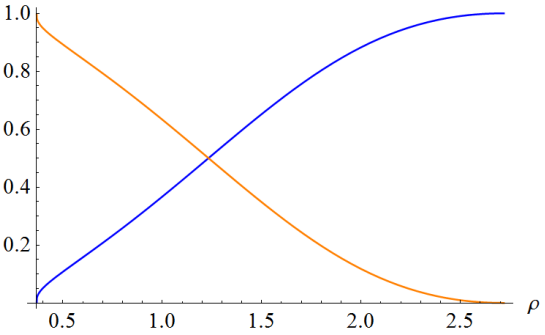

(a) Plot of Φ_+/M_0 (blue) and Φ_-/M_0 (yellow) as functions of $\rho \in (\frac{1}{R}, R) = (e^{-1}, e)$ for $\ell = \pi^2$. The values $\rho = \frac{1}{R}$ and $\rho = R$ correspond to the two funnel ends of $\mathbb{A}(R)$.

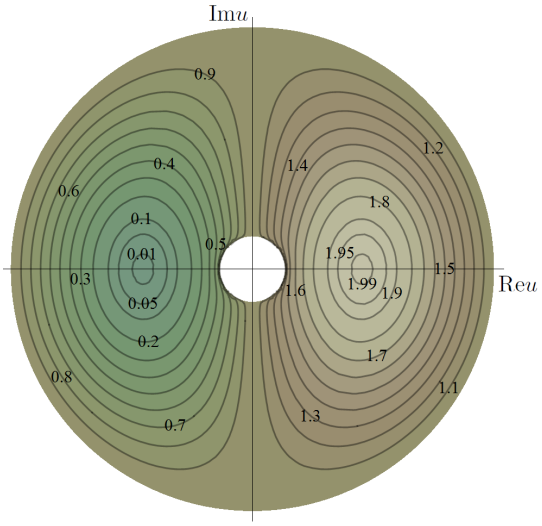

(b) Level plot of Φ_0/M_0 on $\mathbb{A}(R)$ for $\ell = \pi^2$. Darker tones indicate lower values of Φ_0. In this case, the maximum of Φ_0 is located at $u_M = \frac{e^2+e-1}{e^2}$, while the minimum is located at $u_m = -u_M = -\frac{e^2+e-1}{e^2}$.

Figure 14: The potentials $\Phi_\pm$ and Φ_0 on the annulus of modulus $\mu = 2$ ($\ell = \pi^2$, $R = e$). For Φ_+ and Φ_-, we indicate only the dependence of $\rho = |u|$, since these two potentials do not depend on the polar angle θ. Notice that Φ_+ tends to its infimum at the inner funnel end, while Φ_- tends to its infimum at the outer funnel end. Similarly, Φ_+ and Φ_- tend to their suprema at opposite funnel ends.

Lift of $\Phi_\pm$ and Φ_0 to $\mathbb{H}$. The globally well-behaved scalar potentials (6.18) and (6.19) lift to the following potentials on $\mathbb{H}$ (see Figures 15a and 15b):

$$\tilde{\Phi}_+(\tau) = M_0 \frac{1}{1+\left[\log \frac{R-\frac{1}{R}}{\rho(\tau)-\frac{1}{R}}\right]^2} \ , \ \tilde{\Phi}_-(\tau) = M_0 \frac{\left[\log \frac{R-\frac{1}{R}}{\rho(\tau)-\frac{1}{R}}\right]^2}{1+\left[\log \frac{R-\frac{1}{R}}{\rho(\tau)-\frac{1}{R}}\right]^2}$$
$$\tilde{\Phi}_0(\tau) = M_0 \left[1 + \frac{2\log \frac{R-\frac{1}{R}}{\rho(\tau)-\frac{1}{R}}}{1+\left(\log \frac{R-\frac{1}{R}}{\rho(\tau)-\frac{1}{R}}\right)^2} \cos\left(\frac{2\pi}{\ell}\log|\tau|\right)\right] \ , \tag{6.21}$$

where $\rho(\tau) = e^{\frac{\pi^2}{\ell} - \frac{2\pi}{\ell}\arg(\tau)}$ (see (6.15)). The lifted potential $\tilde{\Phi}_0$ has local maxima at the inverse image points of $u_M = +\rho_0$ and local minima at the inverse image points of $u_m = -\rho_0$ (see (6.20)). Using (6.15), we find that these are located at:

- (maxima) $\tau = \tau_M(n) \stackrel{\text{def.}}{=} e^{n\ell + \mathbf{i}\frac{\ell}{2\pi}\log\left(\frac{R}{\rho_0}\right)}$ (where $\tilde{\Phi}_0$ equals $2M_0$)
- (minima) $\tau = \tau_m(n) \stackrel{\text{def.}}{=} e^{(n+\frac{1}{2})\ell + \mathbf{i}\frac{\ell}{2\pi}\log\left(\frac{R}{\rho_0}\right)}$ (where $\tilde{\Phi}_0$ vanishes) ,

with $n \in \mathbb{Z}$ an arbitrary integer. Hence all extrema of $\tilde{\Phi}_0$ lie on the half-line L_0 through the origin which makes an angle $\theta_0 = \frac{\ell}{2\pi}\log\left(\frac{R}{\rho_0}\right)$ with the x axis of the τ-plane. The maxima and minima alternate along this half-line and the ratio between the absolute values of two consecutive maxima or two consecutive minima equals e^ℓ; in particular, the extrema accumulate toward the origin along L_0. The fundamental domain $\mathfrak{D}_\mathbb{H}$ contains exactly one of the minima, namely that located at $\tau = e^{\frac{3}{2}\ell + \mathbf{i}\theta_0}$. On the other hand, the two non-free sides of $\mathfrak{D}_\mathbb{H}$ contain the two consecutive maxima located at $\tau = e^{\ell+\mathbf{i}\theta_0}$ and $\tau = e^{2\ell+\mathbf{i}\theta_0}$; these two maxima of $\tilde{\Phi}_0$ are identified by the projection $\pi_\mathbb{H}$.

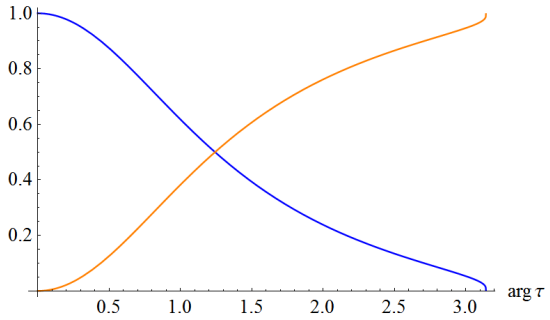

(a) Plot of $\tilde{\Phi}_+/M_0$ (blue) and $\tilde{\Phi}_-/M_0$ (yellow) as functions of $\arg(\tau) \in (0,\pi)$ for $\ell = \pi^2$. The values $\arg(\tau) = 0$ and $\arg(\tau) = \pi$ correspond to the two funnel ends of $\mathbb{A}(R)$.

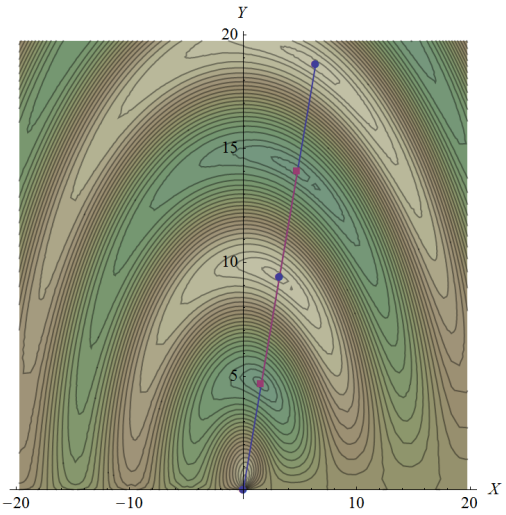

(b) Level plot of $\tilde{\Phi}_0/M_0$ in the coordinates X, Y for $\ell = \pi^2$. Darker tones indicate lower values of $\tilde{\Phi}_0$. The maxima of $\tilde{\Phi}_0$ are indicated as blue dots, while the minima are shown as small red squares.

Figure 15: The lifted potentials $\tilde{\Phi}_\pm$ and $\tilde{\Phi}_0$ for the annulus of modulus $\mu = 2$ ($\ell = \pi^2$, $R = e$).

In Figure 15b, we show the level curves of $\tilde{\Phi}_0$ for the case $\ell = \pi^2$ ($R = e$), which gives $\rho_0 = 1 + \frac{1}{e} - \frac{1}{e^2} \approx 1.23$ and $\theta_0 = \frac{\pi}{2}\left[1 - \log\left(1 + \frac{1}{e} - \frac{1}{e^2}\right)\right] \approx 0.39\pi$. In this case, the absolute value of the ratio of successive minima or maxima of $\tilde{\Phi}_0$ equals $e^{\pi^2} \approx 1.93 \times 10^4$. Due to the large size of this ratio, we chose for clarity to display the level curves of $\tilde{\Phi}$ on a region of the "semi-logarithmic upper half plane". The latter has complex coordinate $T = X + iY$ (where $X = \mathrm{Re}T$ and $Y = \mathrm{Im}T > 0$), being related to the region:

$$\mathcal{R} \stackrel{\text{def.}}{=} \{\tau \in \mathbb{H} \,|\, |\tau| > 1\}$$

of the Poincaré half-plane through the coordinate transformation:

$$T = (\log|\tau|)e^{\mathbf{i}\arg(\tau)} \quad , \quad \tau = e^{|T|}e^{\mathbf{i}\arg(T)} \quad .$$

Notice that $\mathcal{R}$ contains only those extrema of $\tilde{\Phi}_0$ which have absolute value larger than one. In the semi-logarithmic half-plane, these extrema are located at $T = n\ell e^{\mathbf{i}\theta_0}$ with $n \in \mathbb{Z}_{>0}$ (maxima) and $T = (n+\frac{1}{2})\ell e^{\mathbf{i}\theta_0}$ with $n \in \mathbb{Z}_{\geq 0}$ (minima), lying equally-spaced on the half-line in the T-plane which passes through the origin at angle θ_0 with the X axis. The Cartesian coordinates X, Y and $x = \mathrm{Re}\tau$, $y = \mathrm{Im}\tau$ are related through:

$$x = X\frac{e^{\sqrt{X^2+Y^2}}}{\sqrt{X^2+Y^2}} \quad , \quad y = Y\frac{e^{\sqrt{X^2+Y^2}}}{\sqrt{X^2+Y^2}} \quad .$$

Figure 15b shows the level curves of the function $\tilde{\Phi}_0(X,Y)$ in the region defined by $|X| < 2\ell$ and $|Y| < 2\ell$ (where $2\ell = 2\pi^2 \approx 19.7$), which contains the image of the following annular region of the Poincaré half-plane:

$$A \stackrel{\text{def.}}{=} \{\tau \in \mathbb{H} | 1 < |\tau| < e^{2\ell}\} \quad .$$

Notice that A contains a copy of the fundamental domain $\mathfrak{D}_{\mathbb{H}}$.

6.10 Lift of the cosmological model to $\mathbb{H}$

We now present examples of trajectories on $\mathbb{A}(R)$ for $\ell = \pi^2$ ($R = e$, modulus $\mu = 2$) for the vanishing scalar potential and for the globally well-behaved scalar potentials $\Phi_{\pm}$ and Φ_0. These were obtained as explained in Subsection 1.2, by numerically computing solutions of the system (1.3) on the Poincaré half-plane for the corresponding lifted potentials and then projecting these trajectories to the hyperbolic punctured disk using the explicitly-known uniformization map (6.14), which is equivalent with (6.15).

Trajectories for vanishing scalar potential. Figure 16 shows four trajectories (orange, red, blue and magenta) for $\alpha = \frac{M_0}{3}$, $\ell = \pi^2$ ($R = e$) and $\Phi = 0$, with the initial conditions given in Table 1 of Subsection 5.11. In this case, vanishing initial velocity leads to a stationary trajectory (the orange dot), while the hyperbolic geometry produces an effective attraction toward the outer funnel end for $|u| > 1$ and toward the inner funnel end for $|u| < 1$. The red, blue and magenta trajectories start in the funnel region given by $|u| > 1$ (with velocities pointing toward the outer funnel end) and hence evolve toward that end.

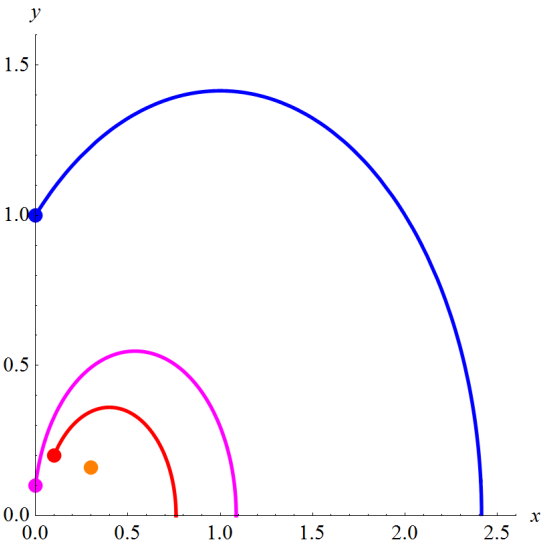

(a) For $\Phi = 0$, the four trajectories on $\mathbb{H}$ with initial conditions given in Table 1 coincide with those shown in Figure 7a.

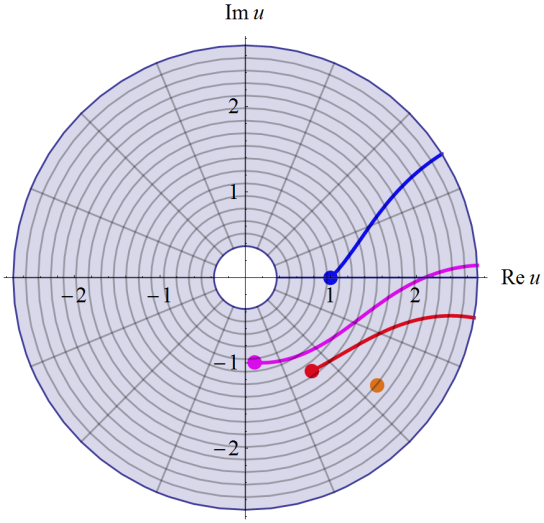

(b) Projection to $\mathbb{A}(R)$ of the trajectories shown at the left. The projection differs from that for $\mathbb{D}^*$ (cf. Figure 7b) since the uniformization maps are different.

Figure 16: Four trajectories for $\Phi = 0$ and $\ell = \pi^2$, with the initial conditions of Table 1.

Trajectories for Φ_-. Figure 17 shows four trajectories (orange, red, blue and magenta) for $\alpha = \frac{M_0}{3}$, $\ell = \pi^2$ ($R = e$) and $\Phi = \Phi_-$, with the initial conditions given in Table 1. In this case, the potential produces a repulsive force away from the inner funnel end, thus accentuating the effect of the hyperbolic metric on the trajectories shown (which start in the outer funnel region).

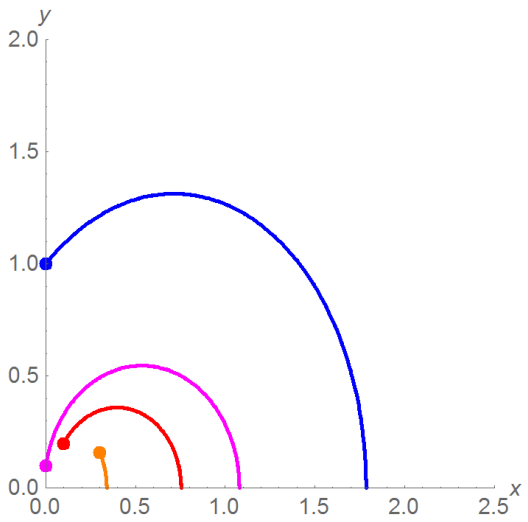

(a) Trajectories on $\mathbb{H}$ for $\Phi = \Phi_-$.

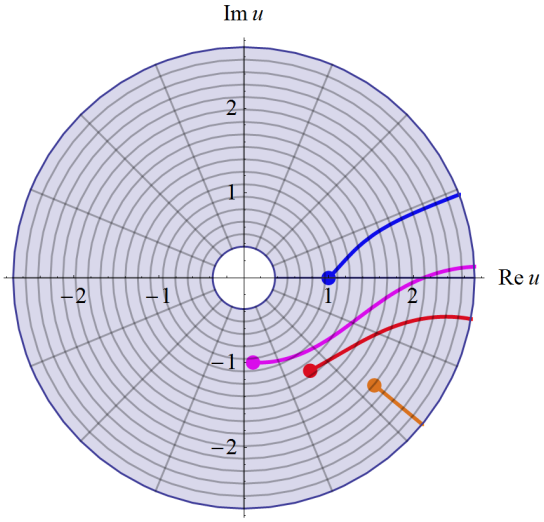

(b) Projection to $\mathbb{A}(R)$ of the trajectories shown at the left.

Figure 17: Four trajectories for $\Phi = \Phi_-$ and $\ell = \pi^2$, with the initial conditions of Table 1.

Trajectories for Φ_+. Figure 18 shows four trajectories (orange, red, blue and magenta) for $\alpha = \frac{M_0}{3}$, $\ell = \pi^2$ ($R = e$) and $\Phi = \Phi_+$, with the initial conditions given in Table 1. In this case, the potential induces an attractive force toward the inner funnel end. As a consequence, each of the red, blue and magenta trajectories turns at some point in $\mathbb{A}(R)$ and evolves back toward the inner funnel end.

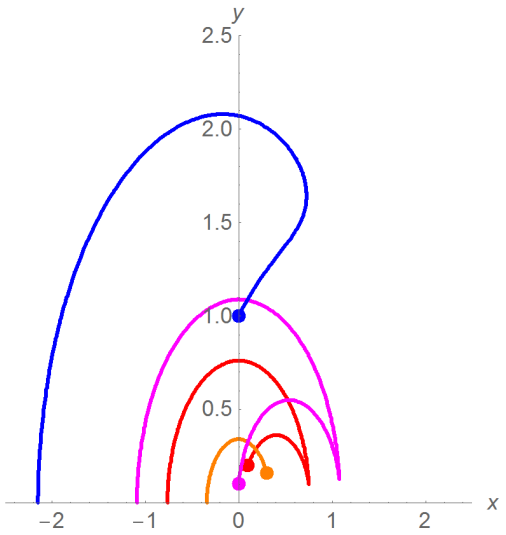

(a) Trajectories on $\mathbb{H}$ for $\Phi = \Phi_+$.

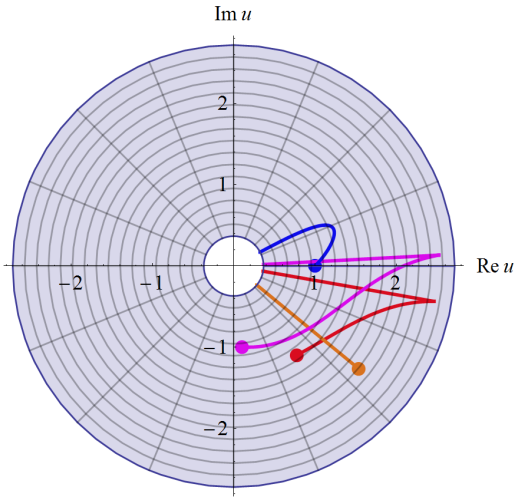

(b) Projection to $\mathbb{A}(R)$ of the trajectories shown at the left.

Figure 18: Four trajectories for $\Phi = \Phi_+$ and $\ell = \pi^2$, with the initial conditions of Table 1.

Trajectories for Φ_0. Figure 19 shows four trajectories (orange, red, blue and magenta) for $\alpha = \frac{M_0}{3}$, $\ell = \pi^2$ ($R = e$) and $\Phi = \Phi_0$, with the initial conditions given in Table 1, as well as another trajectory (green) with initial conditions $\tau_0 = \mathbf{i}e$ and $\tilde{v}_0 = 1 + 10\mathbf{i}$. The lifted green trajectory evolves outside the region shown in Figure 19a, then spirals in a complicated manner around the minimum of $\tilde{\Phi}_0$ corresponding to $n = 0$, which is located at $\tau = \tau_m(0) = e^{\frac{\pi^2}{2} + \mathbf{i}\theta_0} \approx 44.84 + 131.61\mathbf{i}$ and projects to the single minimum of Φ_0 on $\mathbb{A}(R)$ located at $u = -\rho_0 \approx -1.23$. For $t \to \infty$, the trajectory reaches the minimum point (see Figure 20).

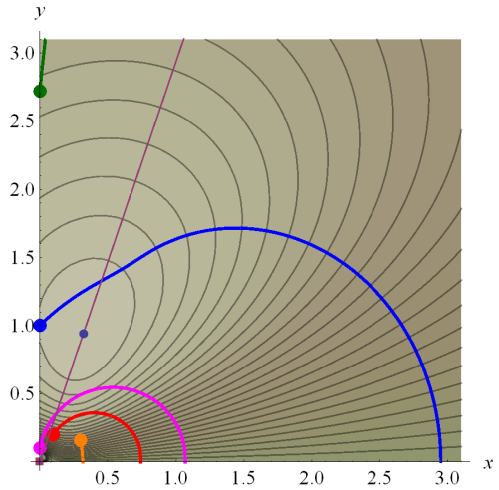

(a) Trajectories on $\mathbb{H}$ for $\Phi = \Phi_0$. Notice that $\tilde{\Phi}$ has a maximum at $\tau = \tau_M(0) \approx 0.32 + 0.94\mathbf{i}$ (indicated by a dark blue dot). The half-line from the origin (drawn in crimson) which passes through this point contains all other extrema of $\tilde{\Phi}$, which accumulate towards the origin. The only extremum which is clearly visible at the scale of the figure is $\tau_M(0)$.

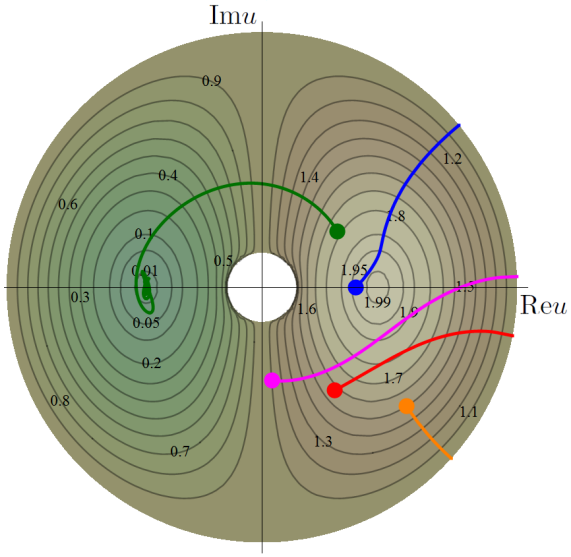

(b) Projection to $\mathbb{A}(R)$ of the five trajectories shown at the left. The green trajectory evolves toward the minimum of Φ located at $u = -\rho_0$, spiraling around that minimum point. All other four trajectories evolve toward one of the funnel ends.

Figure 19: Five trajectories for $\Phi = \Phi_0$ when $\ell = \pi^2$.

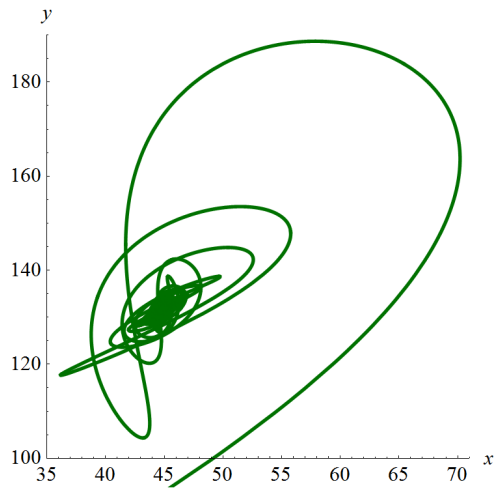

(a) Detail of the lifted green trajectory shown in Figure 19a near the minimum of $\tilde{\Phi}_0$ located at $\tau = \tau_m(0) \approx 44.84 + 131.61\mathbf{i}$.

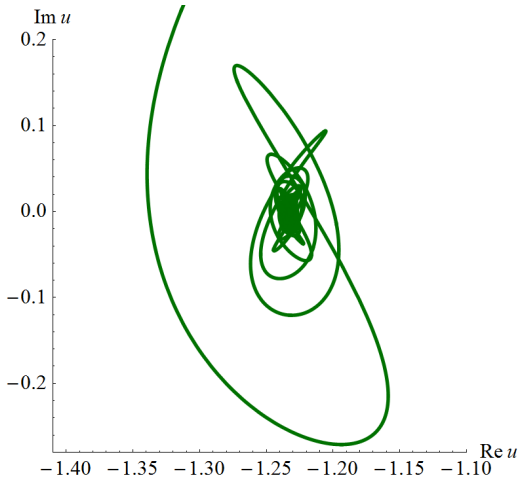

(b) Projection of the trajectory shown at the left to the hyperbolic annulus. The trajectory spirals in a complicated manner around the minimum of Φ_0, until it settles at the minimum point.

Figure 20: Detail of the green trajectory shown in Figure 19.

7 Conclusions and further directions

We studied generalized α-attractor models defined by elementary hyperbolic surfaces, showing how they fit into the framework developed in [1]. Following a "universal" approach to globally well-behaved scalar potentials, we showed how they can be approximated systematically using the Laplace expansion of their extension to the end compactification (which in such models is the unit sphere) and how a smooth real-valued map defined on the latter induces different potentials on each elementary hyperbolic surface. We also illustrated cosmological dynamics of generalized α-attractor models by numerically extracting various trajectories for the cases of $\mathbb{D}^*$ and $\mathbb{A}(R)$, finding rather complex behavior even for relatively simple scalar potentials. From the universal perspective followed here and in [1], the difference between models with globally well-behaved scalar potential defined on various hyperbolic surfaces of the same genus is captured by two maps, namely the uniformization map $\pi_{\mathbb{H}}$ and the map j which embeds the given surface into its end compactification. For elementary surfaces, both of these maps can be constructed explicitly and hence their effects on the cosmological dynamics can be explored systematically.

A similar approach could in principle be followed for any geometrically finite hyperbolic surface. In this regard, it would be natural to explore the large class of non-elementary planar surfaces, which form a classical subject in complex analysis and uniformization theory. For such surfaces, the uniformization map $\pi_{\mathbb{H}}$ is not usually known explicitly and, at least for general values of the moduli, it must be determined numerically. Despite this fact, a fundamental domain is known for any planar surface, as are certain other properties of the hyperbolic metric and of the uniformization map [22, 23]. This allows one to approach generalized α-attractor models whose scalar manifolds are given by such surfaces using the general algorithm proposed in [1, Sec. 7]. For example, it would be interesting to perform a detailed study of cosmological trajectories for some triply-connected non-elementary planar surfaces such as the twice-punctured disk [24–27] and once-punctured annulus [28].

Acknowledgments

The work of M.B. and C.I.L. is supported by grant IBS-R003-S1. The authors thank C. S. Shahbazi for participation in the initial stages of the project.

References

[1] C. I. Lazaroiu, C. S. Shahbazi, *Generalized α-attractor models from geometrically finite hyperbolic surfaces*, arXiv:1702.06484 [hep-th].

[2] R. Kallosh, A. Linde, D. Roest, *Superconformal Inflationary α-Attractors*, JHEP **11** (2013) 098, arXiv:1311.0472 [hep-th].

[3] R. Kallosh, A. Linde, D. Roest, *Large field inflation and double α-attractors*, JHEP **08** (2014) 052, arXiv:1405.3646 [hep-th].

[4] R. Kallosh, A. Linde, D. Roest, *A universal attractor for inflation at strong coupling*, Phys. Rev. Lett. **112** (2014) 011303, arXiv:1310.3950 [hep-th].

[5] M. Galante, R. Kallosh, A. Linde, D. Roest, *The Unity of Cosmological Attractors*, Phys. Rev. Lett. **114** (2015) 141302, arXiv:1412.3797 [hep-th].

[6] J. J. M. Carrasco, R. Kallosh, A. Linde, D. Roest, *The hyperbolic geometry of cosmological attractors*, Phys. Rev. D **92** (2015) 4, 41301, arXiv:1504.05557 [hep-th].

[7] R. Kallosh, A. Linde, *Escher in the Sky*, Comptes Rendus Physique **16** (2015) 914, arXiv:1503.06785 [hep-th].

[8] D. Borthwick, *Spectral Theory of Infinite-Area Hyperbolic Surfaces*, Progress in Mathematics **256**, Birkhäuser, Boston, 2007.

[9] H. P. de Saint-Gervais, *Uniformization of Riemann Surfaces: revisiting a hundred-year-old theorem*, EMS, 2016.

[10] I. Richards, *On the Classification of Non-Compact Surfaces*, Transactions of the AMS **106** (1963) 2, 259–269.

[11] S. Stoilow, *Leçons sur les principes topologiques de la théorie des fonctions analytiques*, Gauthier-Villars, Paris, 1956.

[12] H. Kalf, *On the expansion of a function in terms of spherical harmonics in arbitrary dimensions*, Bull. Belg. Math. Soc. Simon Stevin **2** (1995) 4, 361–380.

[13] A. F. Beardon, *The geometry of discrete groups*, Graduate Texts in Mathematics **91**, Springer, 1983.

[14] S. Katok, *Fuchsian Groups*, U. Chicago Press, 1992.

[15] W. Fenchel, J. Nielsen, *Discontinuous Groups of Isometries in the Hyperbolic Plane*, De Gruyter, 2003.

[16] D. Borthwick, C. Judge, P. A. Perry, *Selberg's zeta function and the spectral geometry of geometrically finite hyperbolic surfaces*, Comment. Math. Helv. **80** (2005) 483–515.

[17] B. Maskit, *Canonical domains on Riemann surfaces*, Proc. Amer. Math. Soc. **106** (1989), 713–721.

[18] A. Haas, *Linearization and mappings onto pseudocircle domains*, Trans. Amer. Math. Soc. **282** (1984), 415–429.

[19] A. F. Beardon, D. Minda, *The hyperbolic metric and geometric function theory*, in "Quasiconformal Mappings and their Applications", eds. S. Ponnusamy, T. Sugawa and M. Vuorinen, Narosa Publishing House, New Delhi, 2007, pp. 10–56.

[20] W. Kuhnel, *Differential Geometry: Curves–Surfaces–Manifolds*, AMS 2015.

[21] A. Gray, E. Abbena, S. Salamon, *Modern Differential Geometry of Curves and Surfaces with Mathematica* (3rd ed.), Chapman & Hall, 2006.

[22] J. A. Hempel, *On the uniformization of the n-punctured sphere*, Bull. London Math. Soc. **20** (1988), 97–115.

[23] T. Sugawa, M. Vuorinen, *Some inequalities for the Poincaré metric of plane domains*, Math. Z. **250** (2005) 4, 885–906.

[24] A. F. Beardon, *The uniformisation of a twice-punctured disc*, Comput. Methods Funct. Theory **12** (2012) 2, 585–596.

[25] J. A. Hempel, S. J. Smith, *Hyperbolic lengths of geodesics surrounding two punctures*, Proc. Amer. Math. Soc. **103** (1988), 513–516.

[26] J. A. Hempel, S. J. Smith, *The accessory parameter problem for the uniformization of the twice-punctured disc*, J. London Math. Soc. **40** (1989) 2, 269–279.

[27] J. A. Hempel, S. J. Smith, *Uniformization of the twice-punctured disc – problems of confluence*, Bull. Australian Math. Soc. **39** (1989), 369–387.

[28] T. Zhang, *Uniformization of a once-punctured annulus*, Computational Methods and Function Theory **15** (2015) 1, 75–91.